NMR Studies of Cathode Materials for Lithium-Ion Rechargeable Batteries

Clare P. Grey* and Nicolas Dupré

Department of Chemistry, State University of New York at Stony Brook, Stony Brook, New York 11794-3400

Contents

1. Introduction

Lithium intercalation or insertion materials have been widely investigated in the search for new electrode materials for use in high-voltage rechargeable batteries.[1–6] The first commercial Li-ion rechargeable battery contains the layered materials $LiCoO_2$ (Figure 1) and graphite as the cathode (or positive electrode) and anode (or negative electrode), respectively.[7] Although this battery is the current standard in many applications including cell phones and laptops, its slow charge and discharge rates and cost have prevented its use in applications that require cheap high power and capacity, such as hybrid electric vehicles and electric vehicles. The toxicity of Co is also an issue. A wide variety of materials have been studied,[5,6] which include doped $LiCoO_2$ phases, layered compounds based on the $LiCoO_2$ structure (e.g., $LiNiO_2$ [8] and $LiNi_{0.5}Mn_{0.5}O_2$ [9,10]),

* To whom correspondence should be addressed. E-mail: cgrey@notes.cc.sunysb.edu.

Clare P. Grey received her B.A. (1987) and D. Phil. (1990) degrees in Chemistry from the University of Oxford. At Oxford she worked with Professors Tony Cheetham and Christopher Dobson on the application of solid-state NMR to problems in solid-state chemistry. She then spent a year as a postdoctoral fellow at the University of Nijmegen in The Netherlands with Professor Wiebren Veeman, where she developed new NMR methods for measuring internuclear distances in systems with quadrupolar nuclei. She was a visiting scientist at the DuPont Experimental Station in Wilmington (1992–1994), where she worked with Dr. Alexander Vega on NMR theory and on the application of NMR to molecular sieves and inorganic–organic composites. She joined the faculty at SUNY Stony Brook in 1994 as Assistant Professor and was promoted to Full Professor in 2001. She uses solid-state NMR spectroscopy, in combination with other characterization techniques such as diffraction, to understand the role that local structure plays in controlling the physical properties of a wide range of materials. Current studies include the investigation of electrode materials for lithium-ion rechargeable batteries, anionic conductors, and ion-exchange and sorption properties of soil minerals, molecular sieves, and layered materials.

Nicolas Dupré was born in Chatillon-sous-Bagneux, France, in 1975. He received his Ph.D. (2001) degree from Université Pierre et Marie Curie–Paris VI working under the direction of Professor Michel Quarton. He was appointed as a postdoctoral associate at SUNY Stony Brook in 2002, where he works with Professor Clare P. Grey. His current research interests are focused on the study of the behavior of materials for lithium batteries using solid-state NMR.
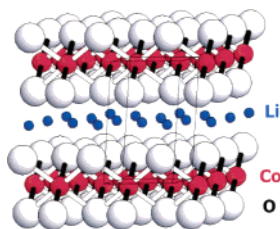
Figure 1. Structure of the cathode material LiCoO$_2$, showing the alternating layers formed by edge-sharing CoO$_6$ octahedra and Li$^+$.

and a series of materials with two- and three-dimensional hosts for Li (e.g., Li$_{1+x}$Mn$_{2-x}$O$_4$ [11] and LiFePO$_4$ [12]). While long-range structural information is typically available from diffraction methods, solid-state NMR is an extremely useful tool for characterizing local structure in these materials, even in highly disordered systems. The lithium nuclei (^{7}Li and ^{6}Li) are typically (but by no means exclusively) used as probes because it is the lithium ions that are directly involved in the electrochemical processes. The NMR spectra are strongly influenced by the electronic structure of the materials, and it is often possible to distinguish between insulators and conductors and between diamagnets and paramagnets. The method is quantitative and can be used to determine which species are removed on charging the battery and how the local structures change on extended cycling. NMR is also sensitive to dynamics that occur on the NMR time scale, and one-dimensional (1D) and two-dimensional (2D) NMR have, for example, been used to investigate Li-ion motion in vanadates (1D)[13] and between two different nanosized domains in anatase, Li$_y$TiO$_2$.[14]

This paper describes the approaches taken by us and other researchers over the past few years to interpret and extract chemical information from this class of materials. We focus on ex-situ analysis of electrode materials (i.e., samples that have been extracted from cycled batteries) since these approaches allow higher resolution spectra to be obtained. Use of a toroid detector (to obtain the NMR signal) has allowed working batteries to be studied in situ by spectroscopy and imaging methods,[15] and more recent studies have shown that NMR signals may be obtained from plastic bag batteries.[16] In-situ methods have not, to date, been combined with the high-resolution method magic angle spinning (MAS) due to a number of experimental difficulties that still need to be surmounted and are, therefore, not discussed here. The theory required to interpret the NMR spectra is first presented (section 2); the use of this theory to extract chemical information is then described (section 3). This is followed by illustrative recent examples from the field. In so far as this is possible, section 4 has been written so that it does not require a detailed understanding of NMR theory (beyond that discussed in section 2.1) and should be accessible to the non-NMR audience. A more comprehensive discussion of some of the technical aspects associated with obtaining NMR spectra of cathode materials can be found in an earlier review article.[17]

2. NMR Background

2.1. Lithium NMR Spectra of Cathode Materials: Introduction

The chemical shift range for lithium NMR spectra is very small, and it is not always possible to resolve resonances due to different local environments in the NMR spectra of diamagnetic materials based solely on the chemical shift interaction. Sometimes improved resolution can be obtained at higher field strengths, allowing chemical information to be extracted from the spectra.[18,19] Fortunately, the lithium NMR spectra of most battery samples are strongly affected by a series of larger interactions which include quadrupole coupling (^{6}Li, $I = 1$; ^{7}Li, $I = 3/2$) and interactions with unpaired electrons for paramagnetic samples (hyperfine interactions) and with the conduction electrons in metals (the Knight shift). ^{7}Li has the much higher natural abundance (93%) and larger quadrupolar and gyromagnetic moments. In contrast, ^{6}Li is only 7% abundant, but its smaller quadrupole and gyromagnetic moments can result in higher resolution spectra that are often easier to interpret. The quadrupolar interaction, which results from the interaction of the quadrupolar nucleus with the electric field gradient (EFG) at the nucleus, is typically very small for ^{6}Li but can result in characteristic broadening in static and a series of spinning sidebands in magic angle spinning (MAS) ^{7}Li NMR spectra due to the satellite ($|+3/2\rangle - |1/2\rangle$ and $|-1/2\rangle - |-3/2\rangle$) transitions. This (anisotropic) interaction contains information concerning the local environments at the lithium nucleus and can be used to distinguish between ions in distorted and more symmetric environments. Many battery materials are paramagnetic in the discharged or charged state. For example, the cathode material LiMn$_2$O$_4$ is a mixed-valence compound containing Mn^{3+} (d^4) and Mn^{4+} (d^3) ions. Although the Co^{3+} d electrons in Li$_x$CoO$_2$ are paired in the fully discharged state, Li$_x$CoO$_2$ contains Co^{4+} d^5 ions when charged. The NMR spectra of paramagnetic materials are dominated by the interactions between the nuclear and electronic spins (Figures 2 and 3). These interactions may be much larger than any of the other interactions and can dominate the spectra of these materials, but they can also contain valuable information concerning both local crystallographic and electronic structure. Hence, we will now consider these interactions in some detail.

2.2. NMR Spectra of Paramagnetic Materials

Paramagnetic ions with electronic spin, S (e.g., $S = 3/2$ for d^3 ions Mn^{4+} and Cr^{3+}), are associated with magnetic moments, μ_e, that align in the presence of a static magnetic field, B_0 (Figure 2), typically defined to be the z-direction. S_z represents the component of the spin along this direction. Electron spin resonance (ESR) probes the transitions between the different spin (or Zeeman) states $|m_s\rangle$. Often the lifetime of an ion in a particular electronic state (T_{1e}) is very short on the relatively long time scale probed by NMR (from many seconds to 10^{-8} s, depending on the size
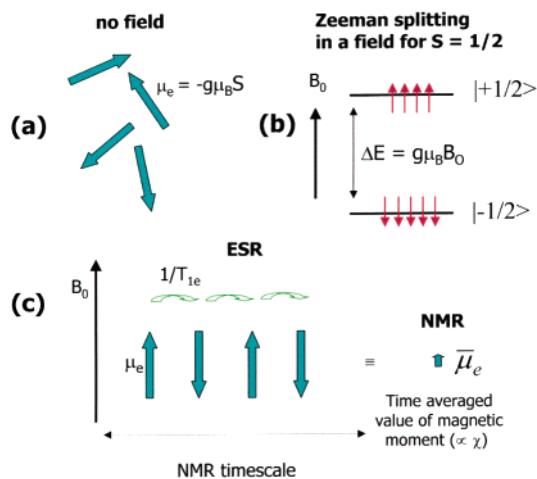
Figure 2. (a, b) Effect of a static magnetic field on a paramagnet with magnetic moment μ_e and electronic spin $S = \frac{1}{2}$. Note that the lowest energy level for $S = \frac{1}{2}$ in the magnetic field is the $|-1/2\rangle$ state due to negative charge of the electron. (The magnetic moment of the electron μ_e associated with this state is still aligned along the direction of the static magnetic field; in many of the subsequent drawings, we will use arrows to represent directions of the net magnetic moments on the electrons/paramagnets.) (c) ESR probes the transitions between the spins states $|+1/2\rangle \leftrightarrow |-1/2\rangle$. Spins in these states relax with a rate $1/T_{1e}$, which is typically much faster than the size of many of the interactions probed by NMR (i.e., T_{1e} is shorter than the NMR time scale). Thus, NMR experiments are generally only sensitive to the time-averaged value of the magnetic moment, $\bar{\mu}_e \ (-g\mu_B\langle S_z\rangle)$.

of the electron–nuclear interaction). In this situation, the NMR spins cannot couple to S_z (i.e., the different spin states $|m_s\rangle$) and instead couple with the time average of the local field, $\langle S_z\rangle$. This is nonzero due to the differences in populations of the different $|m_s\rangle$ states in a magnetic field. The time average of S_z is proportional to the net magnetic moment of an ensemble, which is the quantity measured in a magnetic susceptibility measurement

$$\langle S_z\rangle = -\frac{B_0}{\mu_0 g N_0 \mu_B}\chi_M \tag{1}$$

where μ_0 is the permeability, g the electron g-factor, μ_B the Bohr magneton, N_0 Avogadro's number, and χ_M the magnetic molar susceptibility in $m^3\ mol^{-1}$.[20]

The size of the electron–nuclear interaction can be quantified via a hyperfine coupling constant, A/h (in Hz) (see below), and NMR experiments are feasible for ions with short T_{1e}s, such that[21]

$$|A/h| \ll 1/T_{1e} \tag{2}$$

As the T_{1e}s lengthen and $1/T_{1e}$ (s^{-1}) approaches the size of the electron–nuclear interaction, considerable NMR line broadening can occur, and it may not be possible to acquire high-resolution NMR spectra under these conditions. The effect of T_{1e} on the nuclear relaxation times is discussed in more detail in ref 22. Large hyperfine constants are observed (of many MHz) when the nuclear and electronic spins are on the same atom. For example, a hyperfine constant A/h of -324 MHz was measured by electron
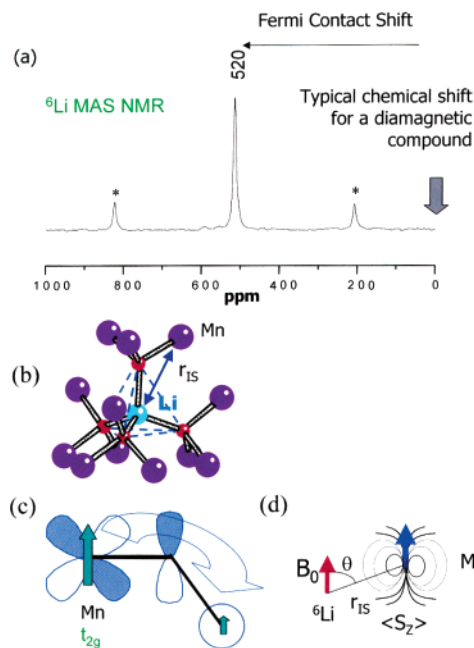

Figure 3. (a) ^6Li MAS NMR spectrum of the spinel LiMn$_2$O$_4$ synthesized at 850 °C acquired with a spinning speed of 10 kHz at a field strength of 4.7 T. The spinning sidebands and the isotropic shift are marked with asterisks and its shift value (520 ppm), respectively. (b) Li local environment in LiMn$_2$O$_4$ showing a tetrahedrally coordinated Li ion and the 12 nearest Mn ions (in the octahedral sites of the spinel structure). Schematics illustrating (c) the transfer of unpaired electron spin density from the unpaired electrons in the t$_{2g}$ d electrons (on one of the 12 nearby Mn ions) via the 2p orbitals on the intervening oxygen atom to the 2s orbital on Li, which causes the large shift seen for the LiMn$_2$O$_4$ isotropic resonance and (d) the dipolar coupling between a ^6Li nuclear spin and net magnetic moment due to a nearby Mn ion. The spinning sidebands shown in (a) primarily result from this interaction, which is not completely removed by MAS.[34]

spin resonance (ESR) for the $S = \frac{1}{2}$ $^{51}V^{4+}$ vanadyl ions in VO(H$_2$O)$_5^{2+}$,[23] and the T_{1e}'s for these ions are $10^{-8}-10^{-9}$ s.[22] $1/T_{1e}$ is similar in magnitude to A/h, and high-resolution NMR spectra are not observed. When the nuclei under observation are further from the paramagnet, A is much smaller (the proton–electron hyperfine coupling constants are only 2.1–0.01 MHz for water molecules in the same vanadyl complex[24–26]) and the condition in eq 2 is more readily achieved. This is the case for lithium spins, which are generally separated by two or more bonds from the paramagnet. In addition, bonding involving Li$^+$ is largely ionic, again reducing the size of A. Shorter T_{1e}s are generally observed for ions with $S > 1/2$ ($S \neq 5/2$), such as Mn^{3+}, Ni^{2+}, and Co^{2+}, and higher resolution spectra are more readily achieved.[22] Broader $^6Li/^7Li$ resonances have been observed for local environments containing the paramagnetic $S = \frac{1}{2}$ ion Ni^{3+} (e.g., for LiNiO$_2$[27] and LiCo$_{1-x}$Ni$_x$O$_2$[28]), but the resonances are not sufficiently broad to prevent detailed analysis of the local environments in these compounds.[28,29]

The nuclear spins can interact with the time-averaged magnetic moments via either through-space (dipolar) or through-bond (Fermi-contact) interactions. The ^6Li MAS NMR spectrum of LiMn$_2$O$_4$ is

presented in Figure 3a to illustrate the effect of the different interactions on the NMR spectrum of this paramagnetic material.

2.2.1. Fermi-Contact Interaction

This is a measure of the unpaired electron spin density that is transferred from the paramagnet to the nucleus of the spin under observation. In the regime defined by eq 2, the NMR shift ($\delta = (\Delta\omega/\omega_0)$) induced by the Fermi-contact interaction is directly proportional to $\langle S_z \rangle$[30,31]

$$\frac{\Delta\omega}{\omega_0} = -\frac{A_c}{\omega_0 h}\langle S_z \rangle \tag{3}$$

The sign (and size) of the hyperfine constant A_c/h (Hz) determines the direction (and size) of the shift

$$A_c/h = g\mu_B\gamma_N\rho(r{=}0)\mu_0/3S \tag{4}$$

and depends on the electron spin (i.e., unpaired electron) density at the nucleus, $\rho(r = 0)$. γ_N is the gyromagnetic ratio for the isotope studied by NMR, and ω_0 is its Larmor frequency (in radians). The $^6Li/^7Li$ hyperfine shift can be very large for many transition-metal oxides and shift the Li resonances well out of the typical range observed in the Li NMR of diamagnetic materials (0 ± 5 ppm) (Figure 3a).

$\rho(0)$ depends on the connectivity between the orbitals on the paramagnet and the orbitals on the NMR-active atom (Figure 3c). Only the electrons in s orbitals are associated with a finite probability of being found at the nucleus, and only the electron density transferred to the s orbitals needs to be considered. Electron density may be transferred either directly from the paramagnet or indirectly via a transferred hyperfine interaction to the s orbitals, and thus, the interaction contains chemical information about the bonding involving the paramagnets, Li, and the intervening oxygen atoms. For example, in $LiMn_2O_4$, the transferred hyperfine interaction will primarily involve the manganese t_{2g}, oxygen 2p, and Li 2s orbitals (Figure 3c). The Fermi contact shift is generally considered to be additive, so that the shift due to many magnetic ions may be obtained from a sum of the shifts induced by each magnetic ion, although exceptions occur in systems with very delocalized spin states. One challenge in this field has been to relate shift to local environment to extract chemical information from these often-complex systems. The correlation between shift and local environment will be explored in some detail in section 3.

The Knight shift, which dominates the spectra of metallic samples, is analogous to the Fermi-contact shift, except that now the shift is a measure of the density of states at the Fermi level, $N(E_f)$. This relationship arises because the Pauli paramagnetism χ_p of a metal is proportional to $N(E_f)$,[32] and thus, since the electron–nucleus interaction is dependent on $\langle S_z \rangle$ and hence χ (eqs 1 and 3), the Knight shift is dependent on $N(E_f)$. Again, since hyperfine coupling requires that unpaired electron density is present at the nucleus under investigation, the Knight shift

depends, to a first approximation, on the contribution of the s orbitals of the NMR-active atom (lithium) to the crystal orbitals with energies at or very close to E_f (i.e., $N(E_f)_{Li,2s}$ the Li 2s partial density of states at the Fermi level; this can be quite different than the value of $N(E_f)$ that is important in controlling the bulk conductivity of the sample). Often the d or p orbitals at the atom under investigation may have larger contributions to $N(E_f)$. This will be the case for some metals and the ^{51}V Knight shifts of vanadates. Here, spin density can also be transferred to the s orbitals via a polarization mechanism and both positive and negative Knight shifts can result, depending on the nature, populations, and locations of the orbitals involved in the process. Polarization mechanisms are discussed in more detail in section 3.1.

2.2.2. Dipolar Coupling

The dipolar interaction is the same interaction that occurs between two or more nuclear moments and is caused by the local magnetic fields of the nuclear or electronic (S) spins that are felt at the nearby nuclear (I) spin (Figure 3d). When the dipolar interaction involves coupling to $S = ^1/_2$ nuclear spins, coupling to both the $|1/2\rangle$ and $|-1/2\rangle$ eigenstates will occur, resulting in the classic Pake doublet pattern for a powder. In contrast, when the second set of coupled spins are electrons (or paramagnetic ions), the nuclear spins can only couple to the time-averaged magnetic moment (again because the electronic relaxation time T_{1e} is extremely fast on the NMR time scale). The line shape in this case resembles that of the chemical shift anisotropy (CSA), and like the CSA, it scales linearly with the field.[33] The Hamiltonian for this interaction, H_{en}, can be represented by[33,34]

$$H_{en} = \frac{\mu_0}{4\pi}\bar{\mu}_e\tilde{D}_{en}\mu_N \tag{5}$$

where $\bar{\mu}_e$ is the time (or thermally) averaged magnetic moment of the electrons (i.e., $-g\mu_B\langle S_z\rangle$) and $\tilde{D}_{en}$ is the dipolar coupling tensor between the unpaired electron and nucleus, which is defined by its matrix elements as follows[35,36]

$$D_{ij} = \frac{1}{r^3}(\delta_{ij} - 3e_ie_j) \tag{6}$$

and depends on both the distance between the nuclear and electronic spins, r (e.g., the Li and Mn atoms in Figure 3b), and the orientation of the interatomic (Li−Mn) vector with respect to the static magnetic field, B_0. δ_{ij} is the Kronecker delta ($\delta_{ij} = 1$ for $i = j$ and 0 for $i \neq j$), e_i and e_j are the x, y, z components of a unit vector pointing from the nuclear spin to the electron spin in a chosen coordinate system. These interactions (and the CSA) are second-rank tensors and therefore averaged by MAS. Since the size of the dipolar interaction is generally larger than the MAS frequency, a series of spinning sidebands result (Figure 3a) that contains information concerning the size of the interaction and the relative orientation of the spins.[37]
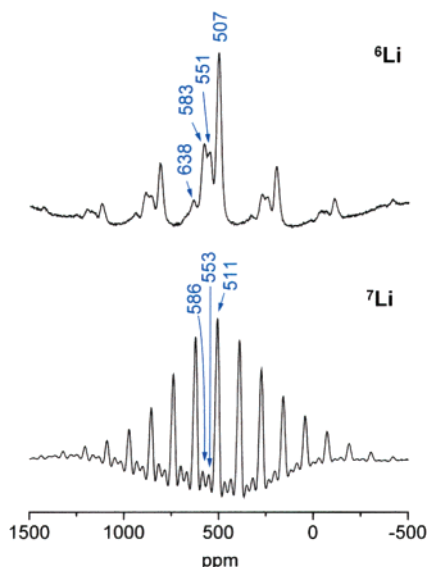
Figure 4. Comparison of the spectra of $LiMn_2O_4$ synthesized at 600 °C obtained with ^6Li and ^7Li MAS NMR at a MAS spinning speed of ~10.5 kHz and a magnetic field strength of 4.7 T (200 MHz for ^1H). (Reprinted with permission from ref 17. Copyright 2003 Elsevier.)

For isotropic magnetic moments, $\bar{\mu}_e$, the interaction results in a line broadening of the resonance only but no overall shift.[38] This will not be the case for an anisotropic magnetic moment. Here, both line broadening and a "pseudo-contact" shift will occur. This is an important mechanism for "shift reagents" in solution NMR and has also been shown to be necessary to explain the ^{89}Y shifts that arise due to lanthanide ions in the solid state.[39] The pseudo-contact shift arises from a similar mechanism as the broadening and line splitting due to a coupling to a quadrupolar nucleus (the interaction involves a fourth-rank tensor). Thus, the line broadening is no longer completely removed by MAS. In many of the batteries studied to date, the size of the shift and line broadening are small and the interaction can often be ignored to a first approximation. More detailed studies are still, however, required to correlate this interaction with line broadening.

The size of the dipolar interaction is often straightforward to calculate as $\langle S_z \rangle$ can be readily estimated from expressions for the susceptibility. For example, assuming spin-only paramagnetism, which is a good approximation for d^3 ions such as Mn^{4+} and Cr^{3+} [40,41]

$$\chi = (\mu_0/4\pi)N_0 g^2 \mu_B{}^2 S(S+1)/3kT \qquad (7)$$

and thus $\bar{\mu}_e$ is given by[42]

$$\bar{\mu}_e = g^2 \mu_B{}^2 S(S+1)B_0/3kT \qquad (8)$$

where k is the Boltzmann constant. In an extended solid, the nuclear spins are typically surrounded by more than one paramagnet and the total Hamiltonian for the dipolar coupling, H_{en}, is obtained by summing the individual coupling tensors for coupling to each individual paramagnetic ions in successive coordination spheres.[34,43]

Since μ_N, the magnetic moment $(=\gamma_N(h/2\pi)I_z)$, depends on the gyromagnetic ratio, γ_N, larger dipolar

couplings are seen for nuclei with larger values of γ_N. Thus, ^7Li with its much larger gyromagnetic ratio than ^6Li $(\gamma_{7Li}/\gamma_{6Li} = 2.6)$ results in MAS spectra with much larger spinning sideband manifolds. Furthermore, unlike the dipolar coupling between nuclear spins, the size of the interaction depends on the magnetic field strength (eq 8). Consequently, the effect of this interaction can be minimized and spectra simplified by using low fields, fast MAS, and nuclei with low γ_Ns. The effect of γ_N is illustrated in Figure 4, which compares the ^6Li and ^7Li spectra of the spinel $LiMn_2O_4$ prepared at 600 °C obtained at an identical spinning speed and magnetic field strength. The sidebands in this system result primarily from the dipolar interactions. Clearly, it is difficult to see all the resonances in the ^7Li spectrum at this spinning speed, and some of the weaker peaks are obscured by the sidebands originating from the more intense resonance at ca. 511 ppm.

3. Extracting Chemical Information from the Spectra of Paramagnetic Materials

3.1. Fermi-Contact Interaction

To extract chemical information from the NMR spectra of paramagnetic battery samples (e.g., Figure 3a), we need to be able to assign a particular value of the hyperfine shift to a specific local environment. To achieve this goal, we[44-47] and other workers[28,48,49] have now studied a series of lithium compounds containing transition metals with electronic configurations from d^1 to d^8. This has allowed us to rationalize the differences in the shift mechanisms that result from the presence of unpaired electrons in the t_{2g} and e_g orbitals of the transition-metal ions. Since the interaction is analogous to the J-coupling that occurs between nuclei and to magnetic interactions between paramagnets, approaches similar to those used in these fields may be used to predict the sign and magnitude of the hyperfine interaction. The correlations developed between the shift and local environment in these lithium NMR studies will now be explored.

To rationalize the large hyperfine shifts observed for lithium manganates such as the spinel $LiMn_2O_4$ (Figure 3a), we synthesized a whole series of compounds within the $MnO_2-LiMnO_2-Li_2MnO_3$ phase diagram. The NMR spectra of these compounds were then acquired to obtain typical hyperfine shift ranges for these materials (Figure 5). Even without a complete understanding of the causes of these large shifts, it then became possible to assign different shift ranges to different lithium local environments. For example, lithium spins in the octahedral site of a Mn^{4+} spinel typically give rise to a resonance at 1800−2300 ppm, while lithium spins in the tetrahedral site of the spinel resonate at ca. 800 ppm. This is illustrated in Figure 5 for the ordered spinel $(Li_{0.5}Zn_{0.5})_{tet}(Li_{0.5}Mn_{1.5})O_4$, which contains Li ions on both the octahedral and tetrahedral sites of the spinel structure. Two resonances are clearly visible, which can be assigned using our hyperfine shift scale to the two different sites in this structure.[50] Similar approaches have been used by us and others to deter-
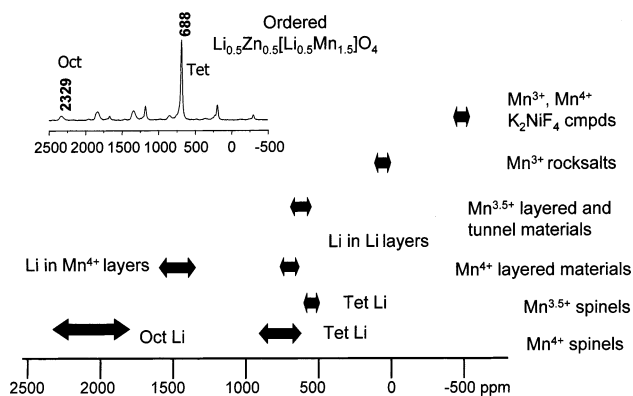
Figure 5. ^{6}Li MAS NMR spectrum of the Mn(IV) spinel $(Li_{0.5}Zn_{0.5})_{tet}(Li_{0.5}Mn_{1.5})_{Oct}O_4$ and the typical hyperfine shifts observed for lithium in a series of local environments. Hyperfine shifts are given next to the two isotropic resonances in the ^{6}Li spectrum; all other peaks are spinning sidebands, which are predominantly caused by the electron−nuclear dipolar coupling.

mine the locations of lithium ions in a series of transition-metal-doped spinels, $LiMn_{2−x}M_xO_4$ (M = Cu, Co, Li, Ni, Cr).[17,51]

We examined the local environments around lithium in a series of Mn(IV) compounds to explain the different hyperfine shifts in these materials. By breaking up the local environments according to the numbers of manganese ions in the first cation coordination sphere around lithium and the Li−O−Mn bond angles, we determined the contribution of each Li−O−Mn interaction to the overall lithium shift.[17,44] This analysis involves two assumptions: (1) that the major shift contribution arises from the hyperfine shift due to manganese ions in the first cation coordination sphere and (2) that there are no significant interactions between paramagnets at the temperatures at which the NMR spectra were acquired (close to room temperature). This latter assumption allows the shifts between different compounds to be compared. (The validity of this assumption can be tested by studying the temperature dependence of the shifts to determine whether there is any evidence for large deviations from Curie−Weiss behavior.[45,46]) For example, one local environment for Li in Li_2MnO_3 contains 12 sets of Li−O−Mn^{4+} bonds, each with a bond angle of close to 90° (Figure 6a). This environment is associated with a hyperfine shift of 1500 ppm or a shift of 125 ppm per Li−O−Mn^{4+} interaction. More generally, Li^+−O−Mn^{4+} bonds with bond angles of 90° were found to result in large positive shifts of ca. 120−150 ppm, while linear Li−O−Mn^{4+} bonds resulted in smaller negative shifts from −60 to −125 ppm, the exact value depending largely on the coordination number of oxygen (Table 1).[47]

The size and direction of the shifts was then rationalized by using the Goodenough−Kanamoori rules, originally designed to predict the sign of the coupling between d electrons in transition-metal oxides. For example, overlap between a half-filled t_{2g} orbital of a manganese ion and an empty 2s lithium orbital in a Li−O−Mn 90° arrangement may occur either directly or via an intervening p orbital on an oxygen atom. In the case of the transferred hyperfine interaction, an interaction with the t_{2g} electron and
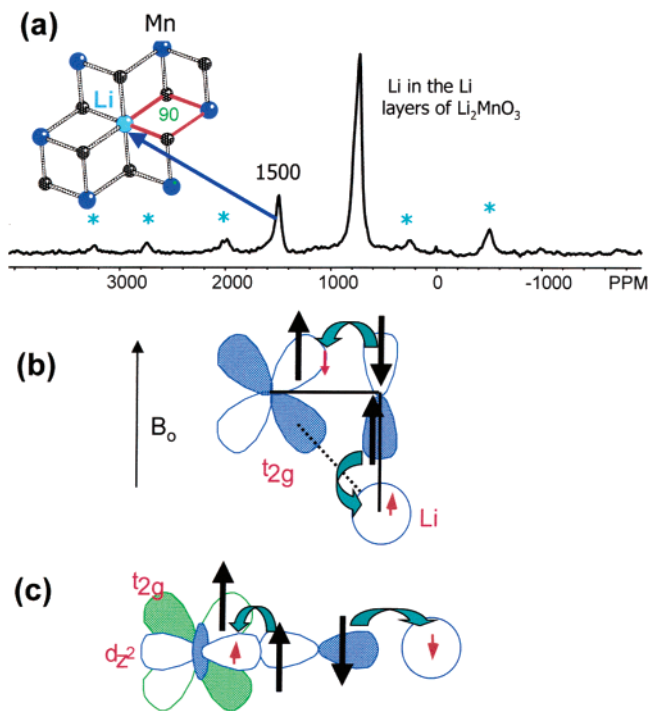

Figure 6. ^{6}Li MAS NMR spectrum of the layered compound Li_2MnO_3 acquired at a MAS frequency, ν_r, of 35 kHz. Spinning sidebands are marked with asterisks. The local environment in the Mn^{4+}/Li^+ layers that gives rise to the isotropic resonance at 1500 ppm is shown. Spin density may be transferred to the 2s orbital of Li via the interaction with (b) a half-filled t_{2g} orbital and (c) an empty d_{z^2} Mn orbital to produce the hyperfine shifts seen in the spectrum of Li_2MnO_3. The large arrows represent the magnetic moments of the electrons in the t_{2g} and p orbitals, while the smaller arrows indicate the sign of the spin density that is transferred to the Li 2s and transition-metal d orbitals.

Table 1. Comparison of the Hyperfine Shifts (in ppm) Observed for Lithium Coordinated to a Single Mn^{4+} Ion via an Intervening Oxygen Ion for a Series of Local Environments[a]

Li−O−M bond angle (deg)	O_{oct} [b]	O_{tet} [c]	O_{linear} [d]
90	122	163	
122		76	
180	−60	−75	−125

[a] Shifts are classified according to the coordination number or environment of the intervening oxygen atom in each Li−O−Mn^{4+} interaction. [b] Li_2MnO_3.[47] [c] Spinel compounds such as $(Li_{0.5}Zn_{0.5})(Li_{0.5}Mn_{1.5})O_4$.[50] [d] Perovskite and K_2NiF_4-related compounds such as $La_2(LiMn)_{0.5}O_4$.[53]

the filled oxygen p orbital can only occur via transfer of spin density of the opposite sign to that already present in the half-filled t_{2g} orbital since the t_{2g} orbital is half-filled (Figure 6b). This then results in transfer of positive spin density to the empty Li 2s orbital and shifts of ca. 120−150 ppm per Li−O−Mn interaction. In the case of a 180° interaction, no direct overlap mechanism is possible involving the t_{2g} orbitals. In this case, the interaction occurs via the empty e_g orbitals (Figure 6c). Here, the exchange coupling between the e_g and t_{2g} orbitals on the same atom favors the transfer of spin density with the same sign of spin polarization as that in the t_{2g} orbitals to the e_g orbitals. This results in a net transfer of negative spin polarization from manganese to the empty 2s
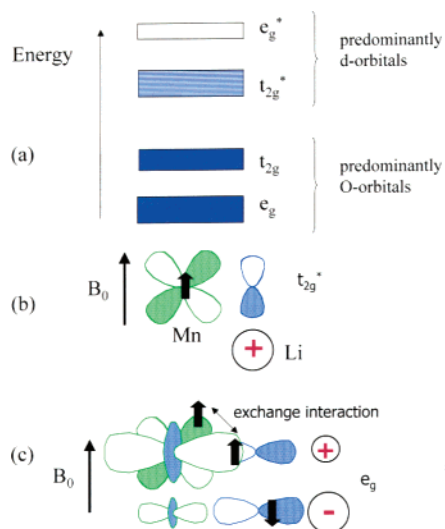
Figure 7. (a) (Partial) band diagram for a transition-metal oxide, with transition-metal ions located in sites with octahedral symmetry. (The t_{2g} and t_{2g}^* crystal orbitals are formed from an overlap of the t_{2g} d orbitals and oxygen 2p atomic orbitals, while the e_g and e_g^* crystal orbitals are formed from the e_g d orbitals and oxygen 2p and 2s atomic orbitals. The t_{2g}^* bands are partially occupied for Mn^{4+} and Cr^{3+} d3 ions.) (b) Delocalization mechanism involving the half-filled t_{2g}^* crystal orbital, and (c) polarization mechanism involving the two one-electron orbitals that make up the "filled e_g orbital". The sizes of orbitals in c represent the relative contributions of these orbitals to the crystal (or molecular) orbital; the sign of the spin-density transferred to the Li 2s orbital is indicated with a "+" or "−" sign.

Li orbital and, consequently, a negative shift. The lithium (tetrahedral) environment in the spinel structure contains 12 Li−O−Mn bond angles of ca. 122° (Figure 3b), and a shift intermediate between that observed for linear and 90° interactions is observed of ca. 76 ppm, as expected, based on orbital overlap arguments. The tetrahedral site in the ordered spinel $(Li_{0.5}Zn_{0.5})(Li_{0.5}Mn_{1.5})O_4$, whose spectrum was shown in Figure 5, contains nine sets of Li−O−Mn bonds with 122° bond angles (the remaining three are Li−O−Li bonds), consistent with the shift for this environment of 688 ppm.

The different shift mechanisms may be understood in more detail by considering the effect of the magnetic field on the populations and energies of the different crystal orbitals (Figure 7a). Transfer of electron density via the 90° interaction arises due to a direct delocalization of spin density due to overlap between the half-filled t_{2g}^*, oxygen π^*, and empty Li 2s atomic orbitals (the delocalization mechanism, Figure 7b).[52] This overlap is responsible for the formation of the t_{2g}^* (antibonding) molecular orbital in a molecule or the t_{2g}^* crystal orbital (or band) in a solid. No shift occurs for the 180° interaction from this mechanism as the e_g^* orbitals are empty.

A second mechanism (the polarization mechanism) arises due to the polarization of the fully occupied (bonding) crystal orbitals formed by the e_g, oxygen 2p, and Li 2s atomic orbitals in the presence of a magnetic field. A fully occupied crystal (or molecular) orbital in reality comprises one one-electron orbital occupied by a "spin-up" electron and a second one-

electron orbital occupied by a "spin-down" electron. This results in the so-called "fully occupied" crystal orbital that contains two paired electrons. In the presence of a field, the energies of the two orbitals are no longer necessarily identical, the one-electron orbital with a magnetic moment aligned with the field being lower in energy. In the case of a "half-filled" orbital, this is the source of the hyperfine shift, as only one out of the two one-electron orbitals is occupied. However, when both of these one-electron orbitals are occupied this does not directly result in a shift. Instead, the shift arises from the effect of the field on the contributions of the different orbitals to the crystal orbitals. In the absence of a magnetic field, the individual one-electron orbitals are identical (i.e., the contributions of the different atomic orbital to the crystal orbital are the same), but this need not be the case when a field is applied. Exchange coupling between electrons in different orbitals lowers the energy of electronic configurations containing parallel electrons. Thus, the presence of "spin-up" electrons in the t_{2g}^* orbitals will stabilize the "spin-up" one-electron orbital formed from the e_g orbitals. This results in a polarization of the e_g crystal orbitals, so that the contribution of e_g atomic orbital to the crystal orbital will be larger for the "spin-up" one-electron orbital and smaller for the "spin-down" orbital. This is illustrated schematically in Figure 7c. Since the "spin-down" orbital is still a one-electron orbital, the contribution to this orbital from the oxygen 2p and Li 2s atomic orbitals must be larger, and thus the concentration of "spin-down" electrons on the Li 2s orbitals is higher than the concentration of "spin-up" electrons, resulting in a net transfer of negative spin density. This picture is entirely equivalent to one where the presence of the magnetic field is considered to mix the e_g and e_g^* orbitals—the extent of mixing is different for the "spin-up" and "spin-down" orbitals, leading to differences in the contributions of the metal d, 2p O, and 2s Li atomic orbitals to the crystal orbitals. A similar phenomenon can occur, for example, in a ferromagnetic solid, the presence of ordered electronic spins acting as the source of the local magnetic field.

The relative sizes of the polarization and delocalization mechanisms will depend on the orbitals involved in the overlap and the occupancies of the metal orbitals. For example, the polarization mechanism appears to be relatively weak for Ni^{3+}, in contrast to Mn^{4+} and Cr^{3+}, even when both mechanisms involve e_g orbitals.[52] This is most likely due to the smaller exchange interaction expected for the Ni^{3+} system, which contains fewer unpaired electrons. Some earlier studies neglected the polarization mechanism, assuming that it was much weaker than the other possible shift mechanisms, which lead to incorrect assignments.[28]

Recent density functional theory (DFT) calculations have been used to calculate the transfer of unpaired electron spin densities to the nearby atoms and analyze the orbitals involved in these mechanisms.[52] For example, Figure 8 shows the spin densities obtained for Cr^{3+}-doped $LiCoO_2$. The spin densities can be calculated by subtracting the "spin-up" elec-
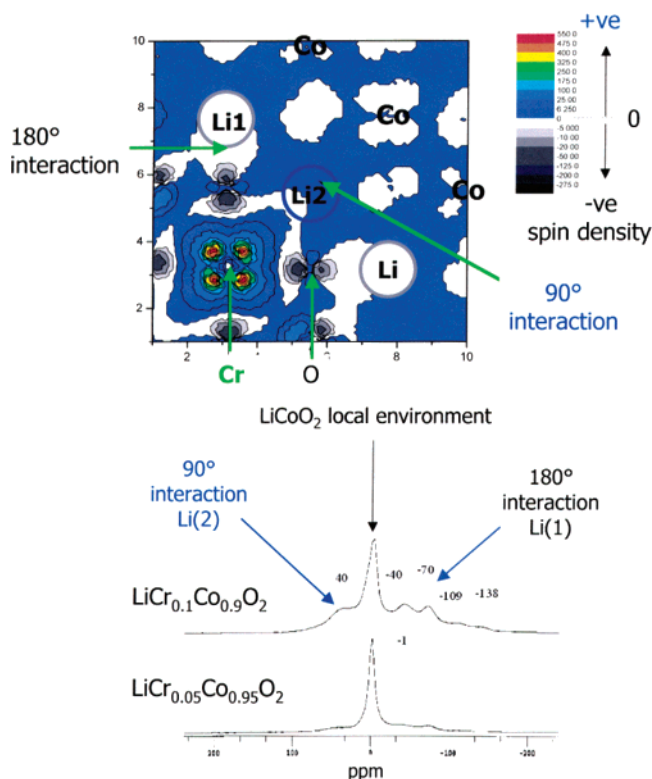
Figure 8. Calculated spin polarization density map in a Co/Cr–O–Li plane in $LiCr_{1/8}Co_{7/8}O_2$ from DFT calculations.[52] The positions of the Cr, Co, Li, and O ions are indicated. Li(1) has a Cr^{3+} ion as its second cation coordination shell, while Li(2) has a Cr^{3+} ion in its first cation coordination shell. The ^6Li spectra of $LiCr_xCo_{1-x}O_2$ ($x = 0.05$ and 0.1)[47] are shown along with the assignments of resonances corresponding to Li(1) and Li(2) local environments.

tron density from the "spin-down" electron density at a particular location in space. The unpaired electron density in the Cr^{3+} (d^3) t_{2g} atomic orbital is clearly visible. Direct overlap of this orbital with a nearby 2p O orbital results in positive spin density in this orbital and positive spin density at the site of the Li nucleus, connected via the 90° interaction. This is consistent with the resonance at 40 ppm seen in the ^6Li NMR spectrum of $LiCo_{1-x}Cr_xO_2$ ($x = 0.1$ and 0.05), which was also assigned to the presence of one Cr^{3+} in the local coordination sphere of a lithium ion. Negative spin density is present in the 2p O orbital that points directly to the Cr^{3+} ion and the Li ion connected via this 180° interaction, consistent with the observation of a resonance at −70 ppm in the NMR spectrum.

Analysis of the spectra of Mn(III) compounds is more complicated as (i) the e_g orbitals are partially filled, (ii) Jahn–Teller distortions typically occur resulting in one half-filled and one empty e_g^* orbital, (iii) many of these compounds contain sizable antiferromagnetic interactions between manganese ions, which result in strong deviations from Curie–Weiss behavior, even at around room temperature. We have analyzed the Mn(III) compounds by examining the Mn–O bond lengths, the longer Mn–O bond lengths (of greater than 2 Å) in the MnO_6 octahedra being indicative of electron occupancy of the (antibonding) e_g^* orbitals. The Mn(III) compound, $La_2(LiMn)_{0.5}O_4$

will be considered initially since this contains isolated manganese ions within the Li/Mn/O planes that are only weakly coupled.[53] $La_2(LiMn)_{0.5}O_4$ is isostructural with K_2NiF_4, and the lithium is coordinated to four manganese ions via linear Li–O–Mn bonds. A shift of −480 ppm was observed for this compound. This is consistent with a Jahn–Teller distortion of the d^4 Mn ions and the population of the e_g^* (d_{z^2}) orbital perpendicular to the Li–O–Mn axes (i.e., perpendicular to the Li/Mn/O planes), so that the Li shift is dominated by the four interactions involving empty $d_{x^2-y^2}$ orbitals. The shift mechanism is similar to that observed for interactions involving empty d_{z^2} orbitals (Figures 6c and 7c).[53]

The three Mn^{3+} rock-salt related compounds with stoichiometry $LiMnO_2$ show much smaller shifts of between 40 and 143 ppm in comparison to the shifts observed for $La_2(LiMn)_{0.5}O_4$ and the Mn(IV) compounds.[45] All the lithium atoms in these compounds have similar numbers of manganese ions in their local coordination sphere, resulting in 12 Li–O–Mn 90° interactions, but differ in the number of types of Li–O–Mn 180° interactions. The slightly larger shifts seen for the tetragonal-$Li_2Mn_2O_4$ and monoclinic-$LiMnO_2$ compounds (99–143 ppm) in comparison to the shift seen for orthorhombic-$LiMnO_2$ (40 ppm) may be rationalized by the presence of additional interactions involving half-filled e_g orbitals, which, for the same reason discussed for the 90° interactions involving t_{2g} orbitals, should result in a positive shift. However, by using arguments outlined above for the Mn(IV) compounds, we would predict a very large shift for these Mn(III) compounds of greater than 1400 ppm. One cause of the large differences is the strong antiferromagnetic interactions between Mn^{3+} ions, which are responsible for non-Curie–Weiss behavior and in the case of o-$LiMnO_2$ for a Néel transition temperature of −11 °C.[54] This suggestion was tested by following the ^6Li shifts of these compounds as a function of temperature.[45] These results demonstrate significant deviation from Curie–Weiss temperature dependence, the shifts being essentially independent of temperature between 0 and 250 °C. Recent density functional theory (DFT) calculations for m-$LiMnO_2$ suggest that changes in bond lengths caused by the Jahn–Teller distortion also strongly affect the relative magnitudes of the different shift mechanisms, resulting in smaller than predicted shifts for these compounds.[52]

These findings are not unique to the manganese systems, and other materials showing strong antiferromagnetic interactions between paramagnets show smaller than predicted shifts. Examples include the NMR spectra of α and β $LiFeO_2$ where shifts of ca. 500 ppm were observed,[27] even though the d^5 Fe^{3+} ions in these compounds contain both partially filled t_{2g} and e_g atomic orbitals. Again, strong deviations from Curie–Weiss behavior are seen for these compounds.

3.2. Dipolar Interaction

Although the sidebands that result from the dipolar interaction can often complicate analysis of the
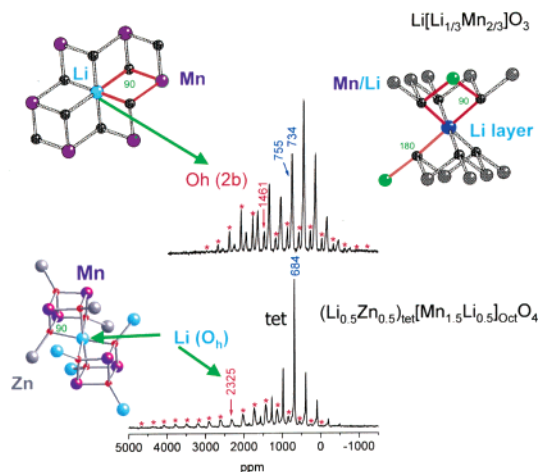
Figure 9. ^{6}Li MAS NMR spectra of the ordered spinel $[Li_{0.5}Zn_{0.5}]_{tet}[Li_{0.5}Mn_{1.5}]_{oct}O_4$ and Li_2MnO_3.[34] The asterisks indicate the spinning sidebands of the resonances from Li in the octahedral site in the spinel and the 2b site of Li_2MnO_3 (i.e., the site due to Li in the Mn layers). The local environments for Li in these sites and the Li in the Li layers of Li_2MnO_3 are shown. These spectra were acquired at a moderately slow spinning speed of 8.7−8.8 kHz (cf. Figure 6) to increase the intensity seen in the spinning sidebands (relative to the isotropic resonance), improving the accuracy of the analysis of the sideband manifolds.

spectrum (Figure 3), this interaction does contain extremely useful structural information that can be relatively straightforward to extract. The effect of different arrangements of paramagnetic ions on the NMR spectra has been explored, and different arrangements can result in characteristic line shapes. This is illustrated in Figure 9 for the two Mn^{4+} compounds Li_2MnO_3 and the spinel $(Li_{0.5}Zn_{0.5})_{tet}(Mn_{1.5}Li_{0.5})_{oct}O_4$. The Li ions in the transition-metal layers of Li_2MnO_3 and in the octahedral site of the spinel are coordinated to the same number of Mn ions (six), but the arrangements of these ions are very different. For Li_2MnO_3, these ions are located in the same plane as the central Li ion (an oblate arrangement), while in the spinel, they lie above and below an imaginary plane running through Li (a prolate arrangement). As discussed above, the total dipolar coupling interaction is a sum of all the individual $Li-Mn^{4+}$ dipolar interactions. The total interaction will be very sensitive to the relative orientations of the Li−Mn interatomic vectors. For the sites in the two compounds discussed here, although the magnitude of the interaction is similar, the sign of the interaction is opposite in sign. Differences in the signs of the interaction result in characteristic changes in the line shapes of the two compounds. The shapes of the sideband manifolds for the two groups of resonances in Li_2MnO_3 (= $Li[Li_{1/3}Mn_{2/3}]O_2$ in the notation used to describe layered compounds) are also very different. Li located in the Li layers is nearby manganese ions arranged above and below the plane of Li ions, and thus the shape of the sideband manifolds of the resonance due to this site is similar to that seen for the octahedral sites in the spinel. The shape is characteristic for Li ions between layers of paramagnetic ions and may be used as a signature for this environment. Much smaller sideband manifolds are seen for the tetrahedral sites, in part because the Li−

Mn distances are larger and also because the ions are arranged more symmetrically around the tetrahedral Li ions so that individual dipolar couplings partially cancel, resulting in a smaller overall dipolar coupling. Again, this smaller dipolar coupling can be used as a signature for the tetrahedral site in these compounds.

4. Applications of NMR Spectroscopy to the Study of Cathode Materials

MAS NMR has now been used to study $LiCoO_2$-derived layered materials[28,29,55] as well as a wide range of alternative cathode materials including manganates,[44,48,49,56−58] vanadates,[13,59−61] and iron and vanadium phosphates.[62−64] We will now discuss the application of NMR to some of these materials to illustrate the type of information that has been (and can be) obtained by using this method.

4.1. Spinels

The spinel materials, $LiMn_{2-x}M'_xO_4$, have been the most extensively investigated of all the lithium manganates.[65,66] These materials can be cycled at ca. 4 V (vs Li) from $LiMn_2O_4$ to MnO_2, the manganese ions retaining the spinel host framework throughout.[1,67] Capacities of 148 mAg^{-1} are, in theory, possible for the stoichiometric spinel, but in practice no more than 100−120 mAg^{-1} has been achieved over multiple charge−discharge cycles.[68] The spinels represent cheap alternative cathode materials which can be charged and discharged sufficiently rapidly to meet the power requirements for use in electric vehicles. Unfortunately, many of the spinels suffer from rapid capacity fade following extended storage or on cycling, particularly at high temperatures.[5] This has prompted much research on these materials to identify the source and then prevent this fade.[69−71] Surface treatment methods have also been developed to help prevent manganese dissolution,[69] and Li-excess spinels $Li_{1+x}Mn_{2-x}O_4$, $x = 0.05−0.1$, are now being produced as cheap cathode materials particularly for use in high-power applications. Figure 10 shows a typical potential profile (obtained in a galvanostatic mode, i.e., by using constant current) for the spinel $Li_{1.05}Mn_{1.95}O_4$.[56] Initial capacities of 125/115 (charging/discharging) mAh/g were obtained (theoretical capacity = 126 mAh/g). Good capacity retention was observed for this material, with 96% of the initial discharge capacity being retained after 30 cycles.

NMR spectroscopy has been performed on these systems to investigate structure before and after electrochemical cycling. A large hyperfine shift of more than 500 ppm from the chemical shift range of typical diamagnetic compounds containing lithium is typically observed in the ^{6}Li or ^{7}Li MAS NMR spectrum of the stoichiometric spinel $LiMn_2O_4$ (Figure 2) synthesized in air at a temperature of between 700 and 850 °C.[44,48,58,72] $LiMn_2O_4$ is a mixed-valent compound containing both Mn^{3+} and Mn^{4+} ions; it is also a hopping semiconductor, hopping occurring between the e_g orbitals of the manganese ions. Since this hopping time scale is fast in comparison to the
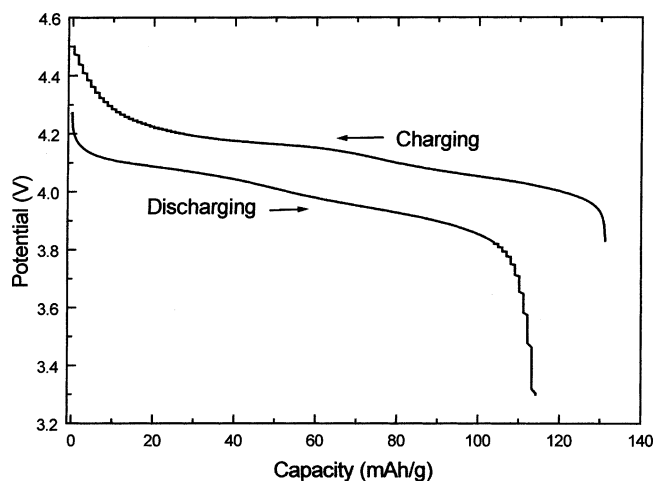
Figure 10. Potential profile of $Li_{1.05}Mn_{1.95}O_4$ during the first charge and discharge in the voltage range of 3.3−4.5 V. The cell (comprising $Li_{1.05}Mn_{1.95}O_4$ as the positive electrode (cathode) and Li as the negative electrode (anode)) was charged/discharged with a constant current corresponding to a charge rate of C/10 (∼10 mA per gram of active material; C/10 indicates that the cell was fully charged in 10 h; a charge rate of 1C corresponds to 1 h). [Similar cells and cycling conditions were used to prepare the samples for the NMR experiments described in section 4.1.1 and in ref 56. Here, cycling was arrested at different potentials, the cells disassembled in a glovebox, and the cathode mixtures packed in NMR rotors.]

NMR time scale (ca. 10^{-5} s), the lithium spins "see" an average manganese oxidation state of 3.5 (i.e., "$Mn^{3.5+}$" ions), and thus there is only one magnetically inequivalent lithium site (the 8a site). The NMR spectra are clearly sensitive to this hopping mechanism, and NMR spectroscopy may be used to follow the partial charge-ordering process that occurs just below room temperature in the stoichiometric material.[44]

In our initial study of these systems[44] we investigated the effect of synthesis temperature on the local structure in the nominally stoichiometric spinel $LiMn_2O_4$, since its stoichiometry and manganese oxidation state depend on the preparation conditions: $Li_2Mn_4O_9$ (Mn^{4+}) may be synthesized at 400 °C,[73] while an increase of temperature results in the formation of defect spinels with a progressive reduction of the manganese oxidation state. Eventually an average oxidation state for manganese of 3.5 is achieved in the stoichiometric material $LiMn_2O_4$ synthesized at ∼850 °C.[74] Figure 11 shows that the ^6Li MAS NMR spectra of this compound vary dramatically with synthesis temperature. Despite the fact that the structure of the stoichiometric spinel contains only *one* crystallographic site for lithium (the 8a site; see Figure 3b), a large number of different *local* environments are observed for the compounds synthesized at lower temperatures. The spectrum of the material synthesized at a temperature of 600 °C resembles the spectrum of samples with excess lithium (e.g., $Li_{1.05}Mn_{1.95}O_4$),[56] which typically show improved cycling behavior.[75−77] Furthermore, a weak resonance at 2300 ppm can be detected in the ^7Li MAS NMR spectra of the materials synthesized at both 550 and 600 °C, collected using an extremely fast MAS spinning speed of 40 kHz.[17]
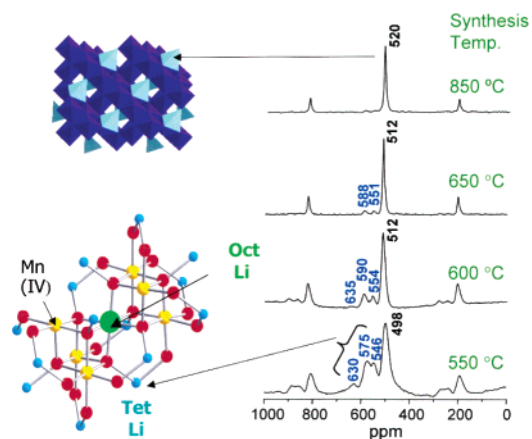

Figure 11. ^6Li MAS NMR spectra of the spinel $LiMn_2O_4$ (structure shown on the left) as a function of synthesis temperature (adapted from ref 44). The cluster of Mn^{4+} ions formed as a result of Li substitution on the octahedral site is shown, and the resonances due to Li ions near this cluster are assigned.

The spinning sideband pattern seen for this resonance is similar to that found for the octahedral site in the spinel $Li_{0.5}Zn_{0.5}[Mn_{0.5}Li_{0.5}]O_4$, confirming that this resonance is due to Li substitution (for Mn) on the octahedral (16d) site of the spinel structure. Thus, the spectra provided clear evidence that the samples prepared at lower temperature contain excess Li, despite their stoichiometry. The residual Mn is presumably present as Mn_2O_3, as shown by Paulsen et al.[78] The additional resonances in the spectra of the nominally stoichiometric material $LiMn_2O_4$ can be assigned by using our hyperfine shift scale (Figure 5) to tetrahedral lithium environments nearby Mn^{4+} ions. These Mn^{4+} ions arise from the substitution of Li^+ in the octahedral (16d) site: For every Li^+ substituted on this site, five $Mn^{3.5+}$ ions must be oxidized to Mn^{4+}. Additional resonances at lower frequency than the main spinel (520 ppm) resonance were observed for spinels prepared above 850 °C or in inert atmospheres.[56] These peaks were ascribed to the presence of Mn^{3+} ions in the Li local coordination sphere, caused by the presence of Mn^{2+} ions on the tetrahedral (8a) site of the spinel structure. Now, the substitution of a Mn^{2+} for Li^+ requires that two $Mn^{3.5+}$ ions are reduced to Mn^{3+} for charge balance.

4.1.1. Cation-Doped Spinels

The Jahn−Teller distortion that occurs on intercalation of $LiMn_2O_4$ to form $Li_2Mn_2O_4$ is associated with a large change in cell volume.[66] One possible source of capacity fade in the spinel material has been ascribed to this Jahn−Teller distortion, which can occur (particularly at the surface of the particles) when the oxidation state of the manganese drops below 3.5 during discharge.[66,79] Doping has been investigated extensively in the spinel system because it represents a method for controlling the oxidation state of the manganese at the end of discharge (of the ca. 4 V plateau).[69] On the basis of charge balance arguments, substitution of a manganese ion for a dopant cation with charge of $n+$ will result in the oxidation of $(3.5 − n)2$ manganese ions with average oxidation states of 3.5 to Mn^{4+}.

The spectra of the doped materials (Cr^{3+}, Ni^{2+}, Zn^{2+}, Li^+, Co^{3+}, Al^{3+}) are similar to those seen for the nominally stoichiometric materials, and sets of resonances between 500 and 700 ppm are seen on cation doping[17,51] in addition to that of the normal spinel environment (at ca. 500 ppm). Again, these resonances are assigned to lithium ions near manganese-(IV) cations. The lower intensity of the additional resonances seen on Cr^{3+} substitution, in comparison to Zn^{2+} or Ni^{2+} substitution, is consistent with the oxidation of fewer manganese ions near the dopart ions. For the Li- and Zn-doped spinels, resonances at ca. 2300 ppm were also observed, which are assigned to lithium ions in the octahedral sites of the spinel structure. In the case of Zn doping, it is clear that the preference of Zn^{2+} for the tetrahedral site of the spinel structure forces the lithium onto the octahedral site.

The NMR results indicate that cation doping does not increase the manganese oxidation states of all cations in the whole phase evenly. Instead, the manganese cations near the dopant cations are oxidized, leaving the bulk relatively unperturbed. This is borne out in the mechanism of deintercalation of these systems, which differs noticeably from the deintercalation mechanism of stoichiometric $LiMn_2O_4$. Two-phase behavior was observed during charging of stoichiometric $LiMn_2O_4$ samples synthesized at 650 °C and above.[80] In contrast, the results for $Li_{1.05}Mn_{1.95}O_4$ (whose potential profile was shown in Figure 10) indicate that the lithium cation is deintercalated from the different local sites sequentially.[56] Li is deintercalated first from the site containing all $Mn^{3.5+}$ ions in its local coordination sphere (ca. 500 ppm); this is followed by Li deintercalation from sites nearby progressively more Mn^{4+}. The resonance at 2100–2300 ppm can be seen throughout the whole charging range studied, indicating the lithium in the octahedral sites is not deintercalated. Li is pinned in the tetrahedral sites near these octahedral Li ions and Mn^{4+} ions. We proposed that the presence of excess Li^+, which serves to pin the tetrahedral Li ions in the lattice, helps to prevent the formation of a series of cation-ordered phases during charging.[56] Instead $Li_{1+x}Mn_{2-x}O_4$ forms a continuous solid–solution on charging and discharging,[81] improving the stability of this material during extended cycling.

On deintercalation of ca. 25% of the Li ions from the tetrahedral site of $Li_{1.05}Mn_{1.95}O_4$, the additional resonances due to Li in tetrahedral sites near Mn^{4+} ions disappear.[56] The fine structure returns on cooling the sample to −60 °C. This indicates that the creation of Li-ion vacancies on charging results in a noticeable increase in Li mobility, involving jumps between the different tetrahedral sites.[56] Verhoeven et al. used 2D ^7Li NMR experiments to study the dynamics of Li in the fully lithiated material $Li_{1.04}Mn_{1.96}O_4$.[57] Their ^7Li NMR spectra are very similar to our ^6Li spectra of a similar material and also the "stoichiometric" material prepared at 600 °C (Figure 11). At temperatures above room temperature, they detected "cross-peaks" in the 2D exchange spectra between the ^7Li resonances at 500–650 ppm, indicating that motion between different Li sites in the

spinel structure was occurring on a millisecond time scale. This was consistent with the complete collapse of the fine structure at higher temperatures in our earlier work, where it was ascribed to either mobility of Li^+ or mobility of the holes on the manganese ions near the defects in these materials (i.e., the octahedral 16d Li ions[17]).[44] Later variable-temperature NMR results for $LiNi_{0.1}Mn_{1.9}O_4$, where similar phenomena were observed, suggested that Li^+ motion must play a role in the collapse of the fine structure.[46] By monitoring the change in cross-peak intensity as a function of temperature, Verhoeven et al. extracted an activation energy for the jump process of 0.5 ± 0.1 eV and also an estimate for the difference in energy between Li in the normal tetrahedral site and Li in the site that gives rise to the resonance at ca. 590 ppm of ca. 700 K (or 0.05 eV). However, their assignments of the spectra are very different from ours.[56] They assigned the two most intense extra resonances at ca. 550 and 590 ppm in Figure 11 (and at slightly higher frequencies in their study) to Li in the 16d (Mn) and 16c sites, respectively. These assignments were made based on the earlier neutron diffraction experiments[82] but, if correct, suggest that the 16c site is occupied in significant concentrations, even at room temperature. The 16c site is an octahedral site which is empty in $LiMn_2O_4$ but is occupied on insertion of Li to form $Li_2Mn_2O_4$.[83] Given our direct observation of the 16d Li site (at 2300 ppm[17]) and that a much larger shift than 590 ppm is predicted for the 16c site, based on our hyperfine shift scale,[44] we suggest that the motion observed here is due to 8a–8a hops, the measured difference in energy between the two sites (0.05 eV) arising from the effect of the Li incorporation into the octahedral (16d) site and formation of the Mn^{4+} ions nearby the "590 ppm" site. The authors suggest that their activation energy corresponds to that of an 8a–16c jump. Most likely, the 8a–8a jump process does occur via the 16c site, the 16c representing a metastable intermediate state. In this case, the measured activation energy still corresponds to that of a 8a–16c hop; however, it seems unlikely that the 16c site is populated for a significant length of time, as implied by this study.

NMR can be used to follow the changes in the electrode materials following multiple charging cycles to determine why some materials fail and others maintain high capacities for extended cycling times. For example, Tucker et al. performed a series of detailed lithium NMR studies to explore the effect of cation doping on the long-term stability of the spinel materials.[49,51] They systematically explored a series of proposed failure mechanisms by preparing model electrode materials where structural changes associated with the proposed failure mechanisms were intentionally introduced. The lithium spectra of the model compounds were then compared with spectra of electrodes extracted from cells that had been charged/discharged for varying numbers of cycles. For example, samples were soaked in moisture-contaminated electrolyte, and the spectra of these were compared to the spectra of the cycled materials. Soaking in wet electrolyte resulted in a shift of the spinel peak to 633 ppm and the appearance of a

resonance at 0 ppm due to the SEI (surface electrode interphase). This shift was not observed in the spectra of the cycled materials. This was in contrast to cells cycled at Stony Brook, where a shift to higher frequency was observed on extended cycling,[80] presumably a consequence of moisture introduced during cell assembly. Both studies ascribed the shift to Mn^{2+} dissolution and the consequent increase in oxidation state of the spinel material which can occur via a reaction such as[84]

$$2LiMn_2O_4 + 4H^+ \rightarrow$$
$$Mn^{2+}(aq) + 3MnO_2 + 2H_2O + 2Li^+(aq) \quad (9)$$
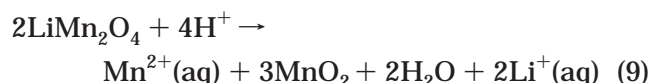
Li^+ loss, but without an increase in manganese oxidation state, can also occur due to ion exchange of Li^+ for any H^+ ions in the electrolyte.[85] Sato et al. showed that the ion-exchange process occurred predominantly on the surface for crystalline spinel samples, the oxidation state of the manganese ions at surface remaining close to 3.5, the average Mn oxidation state of the bulk increasing to 3.9 on treatment with acid.[86] Pickup et al. used Li NMR to examine the effect of chemical delithiation in sulfuric acid solutions on the spinel material.[87] A resonance was observed at ca. 950 ppm for delithiated spinel samples $Li_xMn_2O_4$, $x < 0.3$, which was ascribed to Li in the tetrahedral site in Mn^{4+}-rich domains in the center of the particles. The authors also proposed that these domains resulted from H^+/Li^+ ion-exchange on the surfaces of the particles; the presence of a surface layer of HMn_2O_4 was supported by parallel FTIR studies. The 950 ppm resonance was seen in earlier studies at the top of charge for stoichiometric spinels and following multiple charge−discharge cycles.[80]

An alternative approach for investigating the hydrogen content of cathode materials involves the use of ^2H or ^1H NMR. For example, we showed that ^2H NMR could be used to detect deuterons in samples following chemical or electrochemical reduction.[88] This approach was used to follow the structural changes that occur on acid leaching of Li_2MnO_3.[89] ^2H NMR signals are much easier to detect than ^1H signals because of the much smaller electron−nuclear dipolar couplings involving ^2H due to its smaller γ_N. A ^2H NMR signal from $Li_{1.05}Mn_{1.95}O_4$ soaked in D_2-SO_4 due to ion-exchanged deuterons has been obtained, but no studies following extended cycling have been performed to date.[90]

Finally, NMR has also be used to study other spinels materials that do not contain manganese. For example, the intercalation/deintercalation of lithium titanate spinels such as $Li_{4/3+x}Ti_{5/3}O_4$[91] and $Li_{1.1}$-$Ti_{1.9}O_{4+\delta}$[92] have been investigated. These materials may be used as anode materials in combination with cathodes operating at 4 V (vs Li) to produce cells with potentials of ca. 2.5 V.[93] These materials are either diamagnetic or metallic,[94] and unlike the manganates, only very small differences in shifts are seen for Li in the different sites of the spinel structure. Nonetheless, these shift differences are enough to allow the concentrations of the different sites to be quantified and monitored following insertion of Li[92] or as a function sample preparation method.[94]

4.2. Cr^{3+}- and Ni^{2+}-Substituted Layered Lithium Manganates

Lithium NMR spectroscopy has similarly been applied to investigate the local structure and cycling properties of a number of alternative layered manganese cathode materials. Layered, monoclinic Li-MnO_2 is isostructural with $LiCoO_2$ and has been widely studied as a possible cathode material.[95,96] Unfortunately, this material transforms on cycling at 3−4 V (vs Li) to the more thermodynamically stable spinel phase.[97,98] Cation doping has been used to stabilize the layered phase with some success.[99,100] One series of materials that has generated considerable recent interest includes several cathodes, in particular, containing Ni^{2+} or Cr^{3+} ($Li[Li_{0.2}Mn_{0.4}Cr_{0.4}]$-$O_2$ and $Li[Ni_{0.5}Mn_{0.5}]O_2$) where the charging and discharging cycles involve multiple electron transfers per transition-metal ion.[6,9,10,101] The manganese remains in the +4 valence state at all times, preventing the instabilities associated with Mn^{3+} (i.e., the layered-to-spinel conversion). High capacities of up to 190−220 mAhg^{-1} have been seen for these materials.

Chromium was shown to cycle reversibly between Cr^{3+} and Cr^{6+} in the mixed Cr−Mn oxide $Li[Li_{0.2}$-$Mn_{0.4}Cr_{0.4}]O_2$.[6,102] Lithium NMR spectroscopy showed that the material contains Li_2MnO_3-like and Mn^{4+}-doped $LiCrO_2$ local environments or domains.[47] Only the Li ions in the Mn^{4+}-doped $LiCrO_2$ regions of this "nanocomposite" are removed on cycling and largely responsible for the capacity, while the Li_2MnO_3 parts were inactive. The toxicity of Cr^{6+} restricts the use of this cathode material, and subsequent NMR work has focused on solid solutions of $Li[NiMn]_{0.5}O_2$ and Li_2MnO_3.

Although the widely studied layered material $LiNiO_2$ functions via the reversible cycling of nickel between oxidation states of 3 and 4, nickel may also be cycled between Ni^{2+} and Ni^{4+} at higher voltages in both layered materials and spinels. For example, the spinel $LiNi_{0.5}Mn_{1.5}O_4$ cycles at ca. 4.8 V, the manganese, present as Mn^{4+} in this material, acting as in inert spectator ion.[103] The presence of Ni^{2+} (and not Ni^{3+}) in the spinels $LiNi_xMn_{2-x}O_4$ was clearly demonstrated by NMR.[46] A similar Ni^{2+}/Ni^{4+} process occurs in layered $LiNi_{0.5}Mn_{0.5}O_2$ and its Li-excess versions at a much lower voltage (between ca. 3.7 and 4.6 V).[9,10,104,105]

^6Li NMR has been used to study the local environments in the Li_2MnO_3−$Li(NiMn)_{0.5}O_2$ solid solutions ($Li[Ni_xMn_{(2-x)/3}Li_{(1-2x)/3}]O_2$). Li resonances due to Li ions in the predominantly Li layers (500−800 ppm) and in the transition-metal layers (1360 and 1560 ppm) can be clearly resolved at frequencies close to those seen for similar environments in Li_2MnO_3 (Figure 12).[106,107] Surprisingly, even for the $x = 0.5$ end member, Li ions are still observed in the transition-metal layers (circled in Figure 12), indicating that Ni^{2+}−Li^+ exchange between the layers has occurred. The presence of nickel in the Li layers has been confirmed by diffraction experiments.[104,105] The intensities of the resonances due to Li in the transition-metal layers were used to develop a model for cation ordering and demonstrate that the ordering in these layers was far from random. The Li ions in
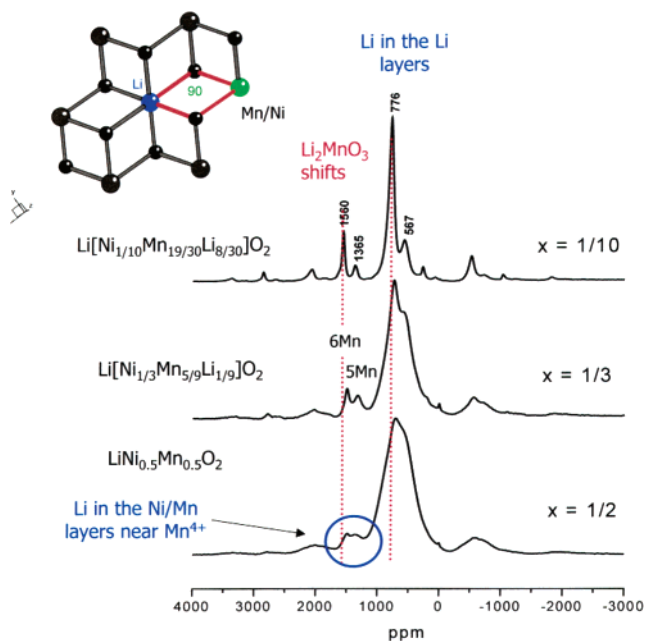
Figure 12. ^{6}Li MAS NMR spectra of Li[Li$_{(1-2x)/3}$Mn$_{(2-x)/3}$-Ni$_x$]O$_2$, with x = 1/10, 1/3, and 1/2. The resonances corresponding to local environments Li(OMn)$_6$ and Li-(OMn)$_4$(OLi$_2$) found in Li$_2$MnO$_3$ are marked. The Li(OMn)$_6$ local environment is shown on the right. The frequencies of the major resonances are indicated; asterisks indicate spinning sidebands.
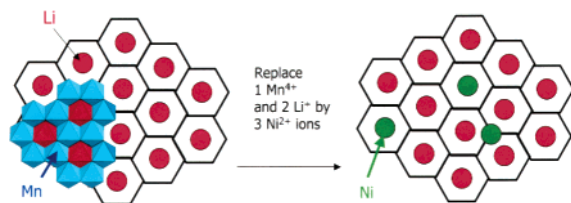

Figure 13. Schematic of the ordering scheme found in Li$_2$-MnO$_3$ showing the honeycomb structure formed by Li (red circles) and Mn (left-hand side) and the structure derived by replacing two Li and one Mn by three Ni (green circles).

the Ni/Mn layers show a strong preference for substitution in environments near six Mn^{4+} ions, as found in the end member compound Li$_2$MnO$_3$. A model was proposed that was based on the "honeycomb" ordering of the Mn^{4+} and Li$^+$ ions in the Mn/Li layer of Li$_2$MnO$_3$, where the Ni^{2+} ions substitute into ordered layers so as to minimize the number of Li$^+$−Ni^{2+} contacts (Figure 13).[107] Studies of these materials following charging and discharging showed that both the Li in the Li layers and in the transition-metal layers participate in the electrochemistry.[106] Even the Li in the Ni/Mn layers can be cycled reversibly at least in the first few cycles.[108] Preliminary results suggest that the Li vacancies created in this process at the top of charge may represent a possible mechanism for creating increased disorder in these materials following extended cycling.

4.3. LiCoO$_2$ and Related Materials

LiCoO$_2$-related cathode materials have been investigated extensively by NMR. The NMR of these systems may be used to follow not only the oxidation of the Co^{3+} and doped ions, but also changes in the electronic conductivities of these materials. In particular, the NMR spectra are extremely sensitive to semiconductor−to−metal phase transitions.[109] Although low-spin d^6 Co^{3+} ions are nominally diamagnetic, the layered (O3) LiCoO$_2$ (Figure 1) and the layered O2 polytype show a very weak, temperature-independent (Van-Vleck) paramagnetism,[110] which is presumably due to mixing in of higher (paramagnetic) states. The labels "O2" and "O3" for the two structures indicate that the Li environment is octahedral in both but that the stacking sequences of the oxygen layers are ABCB and ABCABC, leading to two and three sets of Co and Li layers in the hexagonal unit cell, respectively.

The ^{6}Li and ^{7}Li spectra of the O3 and O2 LiCoO$_2$ phases both show a resonance at −0.2 ppm consistent with lithium in an essentially diamagnetic local environment and the presence of low-spin (t$_{2g}^6$) Co^{3+} ions.[28,110,111] Shift anisotropies, obtained by analysis of the ^{7}Li and ^{6}Li NMR line shapes, were extremely close to those calculated by using the experimentally determined values for the susceptibility χ_m for both phases. ^{59}Co (I = 7/2) NMR has also been used to probe the structure of these materials and extract detailed information concerning the coordination environments in these phases.[110,112] O2 and O3 show quite different ^{59}Co MAS NMR spectra, and the ^{59}Co (I = 7/2) quadrupolar coupling constant (QCC) for the octahedral site in O2 is much larger than that found for the Co site in the O3 material, consistent with the differences in the two structures: the CoO$_6$ octahedra in the O2 structure share a face and three edges with the LiO$_6$ octahedra, while they only share (6) edges in the O3 structure.[110]

NMR spectroscopy has been used to follow the cycling of Li$_x$CoO$_2$.[109] The results indicate that Co^{4+} ions are formed during the initial stages of deintercalation.[109] A broad resonance appears at x = 0.94, the shift being ascribed to a Knight shift, due to interaction between the Li nuclei and the conduction electrons in the t$_{2g}$* band formed from the overlapping t$_{2g}$ cobalt orbitals (Figure 14). The NMR results suggest that the biphasic region that exists in Li$_x$-CoO$_2$ from 0.75 ≤ x ≤ 0.94 is due to this phase transition. Additional ^{7}Li resonances have been seen for Li-excess nonstoichiometric Li$_{1+x}$CoO$_2$, which have been ascribed to the presence of paramagnetic Co^{2+} ions that are formed in conjunction with oxygen and cobalt vacancies.[55] Materials synthesized at higher temperatures have also been shown to contain oxygen vacancies. These oxygen vacancies result in the presence of five-coordinate Co^{3+} ions, the NMR results suggesting that these Co^{3+} ions are not diamagnetic but rather present as so-called "intermediate-spin" Co^{3+} defects.[113]

Lithium NMR has also been used to investigate the Ni^{3+} doping in LiCoO$_2$.[28] A series of ^{7}Li NMR resonances were observed, which correspond to local environments formed by Ni^{3+} substitution in the first and second cation coordination spheres surrounding the lithium ions. The resonances can be assigned by using similar arguments as those used to assign the spectra of the manganates. Recent DFT calculations
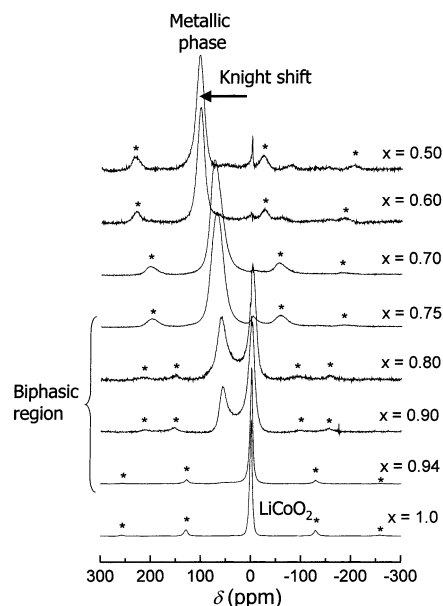
Figure 14. ^7Li MAS NMR spectra for Li_xCoO_2 (asterisks indicate spinning sidebands). The spikes at 0 ppm seen in the spectra of $x = 0.50$ and 0.6 are artifacts. The $LiCoO_2$ local environment and resonance due to the metallic phase are marked. (Reprinted with permission from ref 109. Copyright 1999 Royal Society of Chemistry.)

have shown (in contrast to earlier studies[28]) that the negative shifts seen in these systems are due to Ni^{3+} ions in the Li first coordination shell (90° interactions), while the positive shifts are due to 180° interactions with half-filled e_g orbitals.[52] The large positive shifts are caused by the delocalization mechanism involving the partially filled e_g^* orbitals, while the negative shifts are due to the polarization mechanism now involving the filled t_{2g} orbitals (formed from the metal d_{xy}, d_{xz}, and d_{yz} and the oxygen 2p orbitals) (see section 3.1). These new assignments do not significantly alter the conclusions reached in earlier papers. The distributions of the Ni^{3+} ions and the extent of Ni^{3+} substitution were quantified by extracting the intensities of the different resonances, the results demonstrating that the $LiNi_{1-y}Co_yO_2$ phases have a tendency to form cobalt-rich clusters.[28,29] ^7Li NMR spectra of the partially deintercalated material $Li_xNi_{0.3}Co_{0.7}O_2$, $(1 < x \leq 0.85)$ indicate that the Ni^{3+} ions are oxidized at a lower potential than the Co^{3+} ions, the results suggesting that Ni^{3+}/Ni^{4+} electronic hopping occurs in the early stages of charge. However, at $Li_{0.7}Ni_{0.3}Co_{0.7}O_2$ where in principle all the Ni^{3+} should be oxidized to diamagnetic Ni^{4+}, an NMR signal at ca. 20 ppm is seen. This is not consistent with the presence of only Ni^{4+} and Co^{3+} ions (which are both diamagnetic) and indicates that both Ni^{3+} and Co^{3+} are oxidized in this composition range. Furthermore, the variable-temperature NMR results for this sample suggest that both hopping between both Ni and Co ions occurs (Ni^{3+}/Ni^{4+} and $Ni^{4+} + Co^{3+} \rightarrow Ni^{3+} + Co^{4+}$). Thus, the question as to which ion is being oxidized was suggested to be "irrelevant" in this range. At $x = 0.40$, metallic behavior was seen by NMR (and thermoelectric power measurements) but electronic conductivity measurements showed that the conductivity is still an activated process. The discrepancy was ascribed

to the presence of Ni^{4+} ions, which result in local distortions and prevent full electronic delocalization between Co^{3+} and Co^{4+} ions.[29]

NMR studies have shown that structural defects such as oxygen vacancies and, to a lesser extent, intermediate-spin Co^{3+} are created upon Mg substitution in $LiCoO_2$.[114] ^7Li resonances with noticeable Knight shifts were seen by NMR, even before Li^+-ion deintercalation, but no evidence for metallic conductivity was seen from the electric properties. This was ascribed to the presence of metallic behavior at the local level in small domains surrounding the doped Mg^{2+}. The domains are presumably too well separated and too small to allow percolation (of the conduction electrons) throughout the solid.[114] Doping with other transition metals such as Fe has been also probed by NMR,[115] and the electrochemical properties of the "O2 phase" of $LiCoO_2$ have been investigated in some detail.[116]

Finally, ^{27}Al ($I = 5/2$) and ^{59}Co NMR spectroscopy have been used to probe Al^{3+} in Al-doped lithium cobalt oxides and lithium nickel oxides.[117,118] A ^{27}Al chemical shift of 62.5 ppm was observed for the environment $Al(OCo)_6$ for an Al^{3+} ion in the transition-metal layers, surrounded by six Co^{3+} ions. Somewhat surprisingly, this is in the typical chemical shift range expected for tetrahedral environments (ca. 60–80 ppm), but no evidence for occupancy of the tetrahedral site was obtained from X-ray diffraction and IR studies on the same materials.[117] Substitution of the Co^{3+} by Al^{3+} in the first cation coordination shell leads to an additive chemical shift decrease of ca. 7 ppm, and the shift of the environment $Al(OAl)_6$ (20 ppm) seen in spectra of materials with higher Al content is closer to that expected for octahedral Al. The spectra are consistent with a continuous solid solution involving octahedral sites randomly occupied by Al and Co.[117] It is possible that the unusual ^{27}Al shifts seen for this compound are related to the Van-Vleck susceptibility of this compound.

4.4. Lithium Phosphates

Recently, $LiFePO_4$, which adopts the olivine structure, has been widely studied as a possible cheap cathode material.[12] Although the specific capacities of this material and the related NASICON structures are relatively low (typically 100 mAhg⁻¹), these compounds are cheap and open up new avenues for research. ^7Li MAS NMR studies of a series of olivines $LiMPO_4$ with M = Mn, Fe, Ni, and Co were carried out by Tucker et al.[64,119] A single resonance with large spinning sidebands envelope was observed for all the compounds, indicating the presence of one local environment for the lithium cations. In contrast to the lithium manganese oxide spinels, much smaller shifts from −90 to 70 ppm were seen. The difference between the compounds was rationalized by considering the electronic configuration of the transition-metal cation site in C_s symmetry. Interestingly, the smaller shifts observed in these compounds and in the related vanadium-containing NASICONs[62] is most likely related to the same phenomena that results in the high voltages of these systems (the

Fe^{2+}/Fe^{3+} couple is at 2.8−3.5 V in these structures[120]), namely, the so-called inductive effect of the phosphate groups. The covalent P−O bonds of the phosphate groups will presumably increase the ionic character of the Li−O and M−O bonds in these compounds,[120] reducing the extent of overlap and thus hyperfine interactions in these materials.

4.5. Vanadates

Highly oxidized oxides of vanadium, chromium, niobium, and molybdenum are well known for their ability to intercalate large concentrations of lithium ions on electrochemical reduction.[121−127] Although many vanadium compounds have limited cycle lives in lithium-ion cells, limiting their commercial use, the vanadium oxides V_2O_5, V_6O_{13}, and LiV_3O_8, in particular, are all potential rechargeable 3 V electrode materials and suitable for use in conjunction with polymer electrolytes. These systems have received considerable attention by NMR spectroscopists. In addition to lithium NMR, ^{51}V MAS NMR spectroscopy represents a powerful tool for studying the local environments in these materials, particularly for compounds containing the diamagnetic, d^0 ions V^{5+}. We briefly discuss some of the information that can be obtained from ^{51}V NMR before describing the applications of NMR to these materials.

4.5.1. ^{51}V NMR

The ^{51}V nucleus is quadrupolar (spin 7/2, natural abundance 99.76%), and thus, the spectra can be affected by both the first- and second-order quadrupole interaction, though the second-order broadening is generally not the largest source of line broadening in these materials.[128] In general, three major anisotropic interactions influence the line shapes seen in the ^{51}V NMR spectra of solid samples: (i) the quadrupolar interaction, (ii) the chemical shift anisotropy (CSA), which can be significant for ^{51}V, and (iii) the dipolar interaction between the ^{51}V nucleus under observation and nearby nuclei or electrons. Analysis of the line shapes of these compounds is typically nontrivial, particularly at moderate or high field strengths, and careful simulation of the spectra is required to extract the various parameters describing the CSA (σ_{11}, σ_{22}, σ_{33}) and quadrupolar tensors. The line shapes of the ^{51}V NMR spectra are strongly influenced by the CSA in high magnetic fields and by the quadrupolar interaction in low magnetic fields, and thus, spectra should be acquired at multiple field strengths to ensure accurate measurements of the various interactions.

Although much of the ^{51}V NMR has been performed on model systems or catalytic materials containing vanadium,[129,130] compounds such as V_2O_5 or $VOPO_4$ are used in both the catalysis and lithium battery fields, and many of the results can be used to help elucidate the structures of vanadium-containing cathode materials. ^{51}V NMR spectra are sensitive to changes in the vanadium coordination number and distortions of the vanadium local environments from regular tetrahedra or octahedra.[131−133] ^{51}V isotropic chemical shifts of between −400 and −800 ppm are seen for vanadium oxides, and unfortunately, unlike

^{27}Al and ^{29}Si NMR,[134,135] the isotropic chemical shifts for ^{51}V nuclei in vanadates in different coordination environments overlap. The anisotropy of the chemical shift is, however, sensitive to the arrangement of oxygen atoms in the first coordination sphere: Vanadium atoms in distorted octahedral sites are typically associated with CSAs that are nearly axially symmetric and with spans ($\Delta\sigma = \sigma_{11} - \sigma_{33}$) of ca. 600−1400 ppm. For vanadium atoms in distorted tetrahedral sites, a chemical shift tensor with a large asymmetry parameter η (which indicates the deviation from axial symmetry $\eta = (\sigma_{11} - \sigma_{22})/(\sigma_{iso} - \sigma_{33})$, $0 \le \eta \le 1$; $\eta = 0$ for an axially symmetric tensor) is obtained along with a span of 400−600 ppm. The span drops to 100−300 ppm for a slightly distorted tetrahedral site. The isotropic chemical shift is sensitive to the type of atoms in the second coordination sphere,[136−138] providing additional structural information.

As discussed in section 2.2, ^{51}V NMR spectra of V^{IV} compounds with localized d^1 V^{4+} ions are typically "invisible" by NMR when standard MAS NMR methods are used. In contrast, ^{51}V spectra may be detected for metallic V^{4+} samples,[139] and large shifts are typically observed as a result of the Knight shift. For instance, a large negative Knight shift was observed at −4788 ppm for α-VO_2.[140] ^{51}V resonances for the V^{5+} ions in mixed V^{5+}/V^{4+} compounds may, however, be "visible". A good example is provided by the work of Delmaire et al.,[141] who assigned the resonance at −1447 ppm observed in reduced forms of $Bi_4V_2O_{11-\delta}$ to V^{5+} ions near V^{4+} ions, the large shifts resulting from $V^{5+}-O-V^{4+}$ hyperfine interactions. V_2O_5 does not show metallic behavior on partial or complete reduction of V^{5+} to V^{4+} or V^{3+}. Evidence for partial delocalization of spin density has been obtained for some reduced vanadates by using ESR and NMR spectroscopy, but in these systems delocalization results from a hopping mechanism rather than from metallic behavior.[62,142,143] The main problem associated with the use of ^{51}V NMR to characterize cathode materials is the broadening and/or loss of the signal on reduction, so that it becomes difficult, or impossible, to follow change in the vanadium local environment during lithium intercalation/deintercalation. However, NMR of other nuclei such as $^{6,7}Li$ or ^{31}P can sometimes be performed in parallel to probe these systems.[144,145]

4.5.2. NMR Studies of Vanadium Oxides

The vanadium oxide, V_2O_5, shows particular promise as a positive electrode material in polymer batteries. Because of the existence of the short vanadyl bond,[146] it can either be considered as a two-dimensional layered structure comprising VO_5 square pyramids or a 3D structure formed from VO_6 octahedra. The strong anisotropy of the structure accounts for its ability to accommodate lithium. Intercalation to form $Li_xV_2O_5$ at ca. 3.3 V vs Li^0/Li^+ results in two phases, α ($x < 0.1$) and ε (0.35 < x < 0.7),[147] which differ in their interlayer spacing. δ-LiV_2O_5 is formed after the shearing of the layers.[148] For 1 < x < 2, the δ phase undergoes an irreversible transformation involving considerable reconstruction to form

a γ phase that can cycle between $0 < x < 2$.[149] The intercalation of a third lithium atom into the structure yields the ω phase, which is able to cycle for more than 100 cycles between 3.4 and 1.9 V, yielding a specific energy of 450 Wh/kg.[150]

Numerous studies have been performed using ^{6,7}Li and/or ^{51}V NMR of chemically and electrochemically intercalated V_2O_5 bronzes,[60,143,151] different $Li_xV_2O_5$ phases $(0 < x < 2)$,[152,153] and $Li_xV_2O_5$ aerogels with compositions of $1.00 < x < 5.84$.[62,142] Intercalation of lithium causes distortions resulting in a decrease in the a lattice parameter, an increase in the c parameter (puckering of the V_2O_5 layers[148]), and a change in the coordination of the lithium. Different ^{7}Li MAS NMR resonances are seen for the various lithium sites encountered during electrochemical lithium intercalation: α-$Li_xV_2O_5$ (-16 ppm; trigonal), ϵ_I-$Li_xV_2O_5$/ϵ_{II}-$Li_xV_2O_5$ ($-25/-22$ ppm; trigonal), δ-$Li_xV_2O_5$ (-12 ppm; tetrahedra), γ-$Li_xV_2O_5$ phase (5 and 16 ppm; distorted octahedra and tetrahedra respectively), and ζ-$Li_xV_2O_5$ (10 ppm).[154] The lithium sites in the γ-phase are associated with smaller QCCs, smaller dipolar couplings, and smaller shifts. Sites with low occupancies were more readily seen with ^{7}Li NMR due to its higher sensitivity, while higher resolution spectra were obtained with ^{6}Li NMR.

Hirschinger et al.[143] used NMR to show that the biphasic domain seen on chemical lithiation of V_2O_5 at high temperatures to form lithiated β (^{7}Li NMR resonance at -27 ppm due to monocapped trigonal prisms) and β' (-31 ppm; tetrahedral site) phases should be extended from $x = 0.33$ to 0.48 (at 600 °C).[155,156] The unpaired electrons become increasingly delocalized as the lithium content decreases in the β/β' phases, in contrast to the γ phase, where the electrons were localized on specific vanadium sites.

Stallworth et al. showed that the Li sites in V_2O_5 aerogels occupy sites with axial symmetry, consistent with proposed structural models where the intercalated lithium ions are situated at the apical oxygen position between adjacent V_2O_5 layers.[62,142] New sites are occupied on incorporation of larger amounts of lithium, which are associated with nonbridging oxygens in the equatorial plane of the VO_5 unit. ^{51}V NMR resonances were seen for all the reduced samples, allowing the V^{4+}/V^{5+} ratio to be evaluated.

In addition to structural information, ^{7}Li MAS NMR T_2 relaxation measurements and analysis of ^{7}Li line shapes have been used to probe the dynamics of the lithium ions.[13,153] Holland et al.[13] identified two different species with different mobilities (interfacial Li (longer T_2, rapid dynamics) and intercalated lithium (shorter T_2, slower dynamics)) in the electrochemically lithiated V_2O_5 xerogel matrix. Li hopping frequencies were extracted from an analysis of the ^{7}Li line widths and the appearance of a quadrupolar splitting as the temperature decreased in a related system.[153]

$Li_{1+x}V_3O_8$ has received considerable attention as a cathode material for secondary lithium batteries over the past few years.[157−162] $Li_{1+x}V_3O_8$ has a layered framework suitable for reversible lithium intercalation processes that can allow up to four Li^+ ions per formula unit to be inserted (i.e., x can vary from 0 to
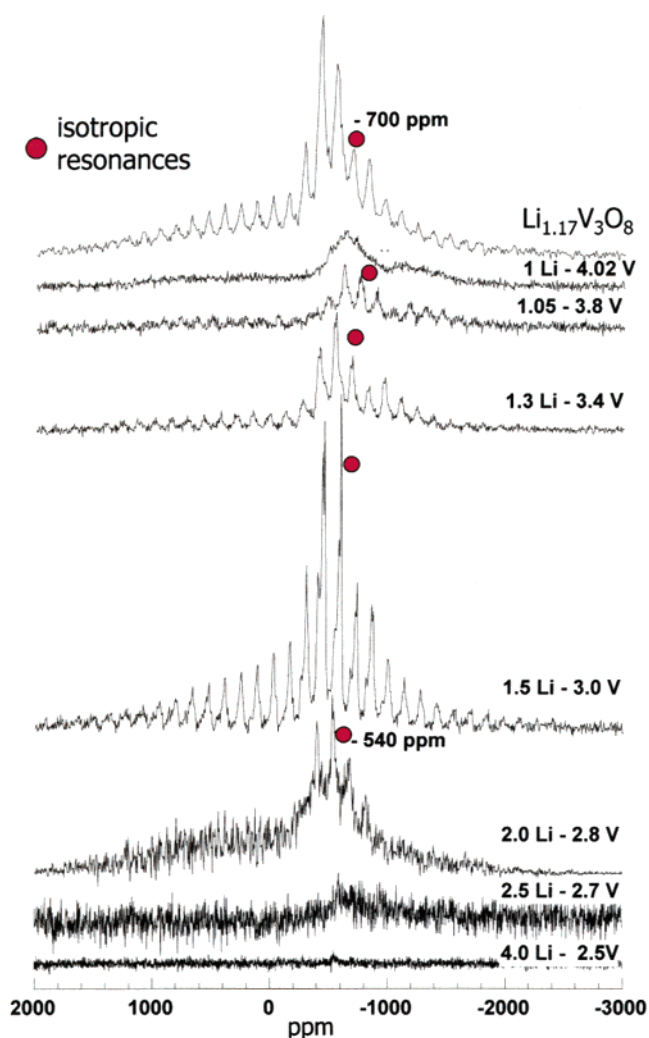

Figure 15. ^{51}V MAS NMR spectra of $Li_{1+x}V_3O_8$ obtained at different stages of the intercalation process ($\nu_r = 13$ kHz), plotted in a quantitative mode. The isotropic resonances are marked with circles.

4). The compound forms a continuous solid solution between 4.2 and 3.0 V and shows two reversible phase transitions at lower potential during cycling. The V_3O_8 layers of LiV_3O_8 are comprised of vanadium in square pyramids (V1), distorted octahedra (V2), and more regular octahedral (V3).[160] Experimental and theoretical studies performed by Benedek et al.,[161] Picciotto et al.,[159] and Jouanneau[162] suggested a number of different possible (octahedral and tetrahedral) sites for Li.

Both the ^{51}V and ^{7}Li NMR spectra show multiple vanadium and lithium local environments for the as-synthesized material ($x = 0.15$), and the spectra cannot be explained by using a simple model[145] based on the number of crystallographically distinct vanadium sites.[159,161] On Li-ion intercalation, the ^{51}V resonances sharpen and shift to higher frequencies (Figure 15); three sharp resonances along with two broader resonances are clearly resolved for the samples prepared at potentials of 3.4 and 3.0 V ($x = 0.3$ and 0.5, respectively). This behavior is consistent with solid−solution behavior in this potential range and is ascribed to the presence of localized V^{4+} defects at x close to 0 and electron delocalization for $1 > x > 0.05$. Three lithium sites were observed in the ^{7}Li

NMR spectra for $0 < x < 1$, which are assigned to the octahedral site and two tetrahedral sites between the lithium layers. A phase transition has been seen in the electrochemical data at ca. 2.8 V to form $Li_2V_3O_8$, but no evidence is seen for this transition with structural probes (such as diffraction and transmission electron microscopy). The phase transition results in a dramatic change in the NMR spectra. A noticeable decrease in intensity and resolution of the ^{51}V resonances is seen, which has been ascribed to a first-order electronic transition with charge ordering and the formation of localized V^{4+} and V^{5+} ions. The lithium NMR spectra are similarly consistent with localized paramagnets. Small negative shifts are seen, consistent with the presence of d electrons in the d_{xy} orbitals of the vanadium ions.

Lithium intercalation in V_6O_{13} has been studied by Stallworth et al.[60] Variable-temperature ^7Li NMR indicated considerable mobility for Li^+ in the intercalated materials. The ^7Li NMR data were compared with ESR spectra and near-edge X-ray absorption fine structure (NEXAFS) data on the same materials, and a correlation between vanadium oxidation state (from NEXAFS data) and NMR shift was observed. The authors explained the shifts in terms of different coupling mechanisms between the V^{4+} and V^{3+} shifts. The shifts were, however, extracted from static NMR experiments, and it is possible that some of the different local environments, typically revealed in a MAS spectrum, were not seen in this study.

4.5.3. Vanadium Phosphates

More recently, lithium vanadium phosphates ($Li_3V_2(PO_4)_3$ and $Li_3FeV(PO_4)_3$,[163,62] with open NASICON framework structures, have also been studied. Reversible electrochemical lithium deintercalation/reintercalation at a higher potential (in comparison to the V^{5+}/V^{4+} couples seen for the oxides) of between 3 and 3.5 V (vs Li^0/Li^+) is seen along with high lithium diffusion rates. $VOXO_4$ materials (X = S, P, As)[164−167] contain two- or three-dimensional frameworks[168−170] that can accommodate lithium. They have high theoretical specific capacities (from 135 to 165 mAhg^{-1}, depending on X), reversible Li intercalation occurring at a potential of ca. 4 V for β-$VOPO_4$[165] and at 3.5−3.7 V for α_{II}-$VOPO_4$.[166,167]

^{51}V, $^{6,7}Li$, and ^{31}P MAS NMR spectroscopy have been performed to study the two first electrochemical cycles of α_{II}-$VOPO_4$ and β-$VOPO_4$.[144] Lapina et al.[171] and Siegel et al.[172] determined both the magnitude and relative orientation of the quadrupole and chemical shift tensors for the α_I-, α_{II}- ($\delta_{iso} = -755$ ppm), and β-$VOPO_4$ ($\delta_{iso} = -735$ ppm) phases from ^{51}V NMR data with slightly different results being obtained between the two groups for the α_{II} phase. $^{6,7}Li$, ^{31}P, and ^{51}V magic angle spinning (MAS) NMR were used to follow the evolution of α_{II}-$VOPO_4$ during the two first electrochemical cycles. Lithium intercalation in α_{II}-$VOPO_4$, to form α_{II}-$LiVOPO_4$, occurs in two voltages on the first reduction, at 3.7 (16% of the total capacity) and 3.5 V (84% of the total capacity), resulting in a ^6Li resonance at 120 ppm (Figure 16) characteristic of α_{II}-$LiVOPO_4$. The subsequent lithium deintercalation occurs in three steps, all of them

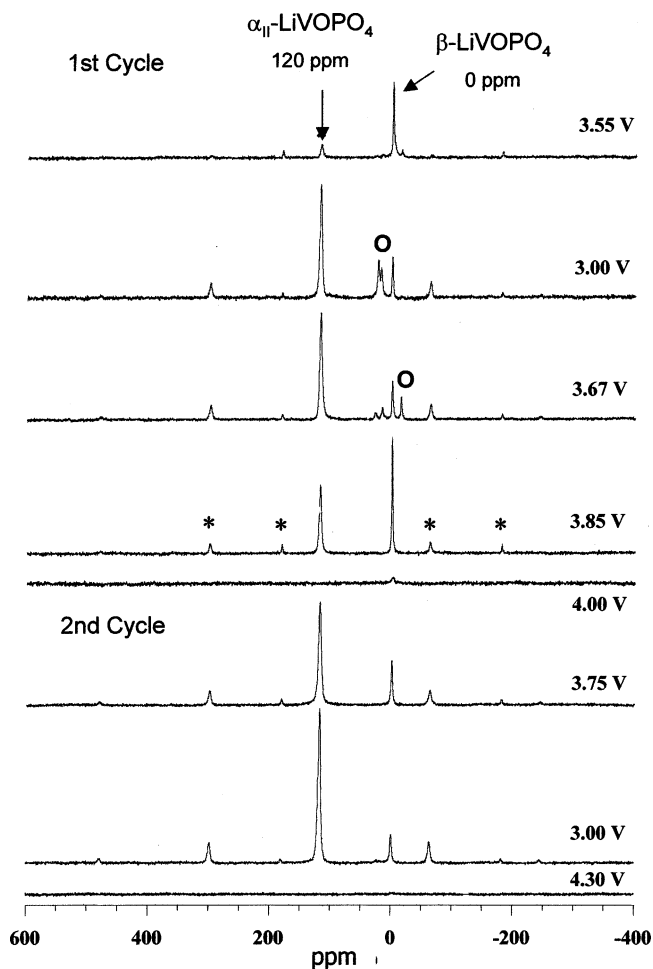**Figure 16.** Quantitative ^6Li MAS NMR spectra of α_{II}-Li_x-$VOPO_4$ acquired during the first and second electrochemical cycles at $B_0 = 7.1$ T ($\nu_r = 8.0$ kHz). The shifts of the isotropic resonances are marked next to the peaks. The circles and asterisks indicate extra impurity peaks and sidebands, respectively.

involving the α_{II} phase, at 3.5 (26%), 3.7 (16%), and 3.9 V (58%), while the second lithium intercalation takes place in two steps at 3.9 (75%) and 3.7 V (25% of the total capacity). These changes reflect an electrochemically driven structural rearrangement that occurs upon cycling of α_{II}-$VOPO_4$, which leads to a change in the lithium intercalation/deintercalation potential. This transformation was proposed to involve local rearrangements of ions as well as the nucleation and growth of well-defined phases. A ^6Li signal corresponding to the β phase, present as an impurity, is seen even at high potentials (3.75 V) at 0 ppm.

Only the nonlithiated diamagnetic phase may be seen by ^{51}V NMR, lithium intercalation resulting in a dramatic loss of signal, presumably due to the large ^{51}V−electron hyperfine interaction (as discussed in section 2.2), the ^6Li NMR resonance at 120 ppm confirming the presence of V^{4+} ions. Thus, the method cannot be used to follow the lithium intercalation into the different sites in the host structure. The percentage of β phase (12%) present as an impurity could be extracted from the ^{51}V MAS NMR spectrum. The signal corresponding to the β phase disappears at the beginning of the discharge but reappears at the end of the cycle, at high potential (4.0 V), showing that

the α_{II} and β phases cycle independently. The intensity of α_{II} phase decreased as a function of cycle number, suggesting that other paramagnetic phases are formed; this is confirmed by observation of additional resonances in the ^{6}Li and ^{31}P MAS NMR spectra of the same materials.

No ^{51}V NMR studies have been performed on the rhombohedral form of $Li_{3-x}V_2(PO_4)_3$ due to the localization of electrons on the V^{4+} and V^{3+} ions. ^{7}Li NMR experiments have however been performed on this system, which suggest that ions on the M(3) sites of the NASICON structure in $Li_3V_2(PO_4)_3$ move onto the M(1) sites on extraction of Li to form $LiV_2(PO_4)_3$.[62] A shift of the isotropic resonance from 85 to 62 ppm on deintercalation of two Li^+ ions is attributed to the change in site geometry and the change in vanadium oxidation state from V^{3+} to V^{4+}. Finally, ^{7}Li NMR studies performed on the monoclinic form of Li_xV_2-$(PO_4)_3$ provide strong evidence for Li and vanadium charge ordering on insertion of lithium, the ordering driving the series of phase transitions seen for this material.[173]

5. Conclusions

NMR represents a powerful method for studying the local structures and electronic properties of cathode materials as a function of state of charge. The research reviewed in this article clearly demonstrates that it is now possible to obtain a wealth of information from the NMR spectra of cathode materials, even in the paramagnetic or metallic state, both prior to and following electrochemical cycling of a battery. The paramagnetic properties of many of these systems, rather than being a complication, can often provide increased resolution of resonances from different local environments. The lithium hyperfine shifts of many systems can be rationalized in terms of the coordination environment for lithium and the numbers and types of unpaired electrons on the nearby paramagnets. In the case of systems whose hyperfine shifts obey a Curie–Weiss Law, it is often possible to predict the magnitude and direction of the shifts by analyzing the connectivity between lithium and nearby paramagnetic ions.

NMR may be used to probe the effect of doping on local structure. For example, NMR studies of the spinel phases show that cation doping results in an increase in the oxidation state of the manganese ions near the cation dopant, while cation doping in $LiCoO_2$ has a dramatic effect on the electronic structure of the material. NMR may be used to determine the cation ordering and investigate the effect of local structure on the electrochemical properties of the cathode materials. In phosphates and vanadates, additional probes such as ^{51}V and ^{31}P NMR provide additional information concerning local structure and electronic properties. In conclusion, NMR has now been applied to a wide range of cathode materials for lithium-ion batteries and is rapidly becoming an essential characterization tool in this research area.

6. Acknowledgments

7. References

(1) Bruce, P. G. *Chem. Commun.* **1997**, 1817.
(2) Guyomard, D.; Tarascon, J. M. *Solid State Ionics* **1994**, *69*, 222.
(3) Koksbang, R.; Barker, J.; Shi, H.; Saidi, M. Y. *Solid St. Ionics* **1996**, *84*, 1.
(4) Winter, M.; Besenhard, J. O.; Spahr, M. E.; Novak, P. *Adv. Mater.* **1998**, *10*, 725.
(5) Tarascon, J.-M.; Armand, M. *Nature* **2001**, *414*, 359.
(6) Ammundsen, B.; Paulsen, J. *Adv. Mater.* **2001**, *13*, 943.
(7) Nagaura, T.; Tozawa, K. *Prog. Batteries Solar Cells* **1990**, *9*, 209.
(8) Dahn, J. R.; von Sacken, U.; Michal, C. A. *Solid State Ionics* **1990**, *44*, 87.
(9) Ohzuku, T.; Makimura, Y. *Chem. Lett.* **2001**, 744.
(10) Lu, Z.; MacNeil, D. D.; Dahn, J. R. *Electrochem. Solid State Lett.* **2001**, *4*, A191.
(11) Thackeray, M. M.; David, W. I. F.; Bruce, P. G.; Goodenough, J. B. *Mater. Res. Bull.* **1983**, *18*, 461.
(12) Padhi, A. K.; Nanjundaswamy, K. S.; Goodenough, J. B. *J. Electrochem. Soc.* **1997**, *144*, 1188.
(13) Holland, G. P.; Buttry, D. A.; Yarger, J. L. *Chem. Mater.* **2001**, *14*, 3875.
(14) Wagemaker, M. M.; Kentgens, A. P. M.; Mulder, F. M. *Nature* **2002**, *418*, 397.
(15) Gerald, R. E.; Sanchez, J.; Johnson, C. S.; Klinger, R. J.; Rathke, J. W. *J. Phys. Condens. Mater.* **2001**, *13*, 8269.
(16) Chevallier, F.; Letellier, M.; Morcrette, M.; Tarascon, J.-M.; Frackowiak, E.; Rouzaud, J.-N.; Béguin, F. *Electrochem. Solid-State Lett.* **2003**, *6*, A225.
(17) Grey, C. P.; Lee, Y. J. *Solid State Sci.* **2003**, *5*, 883.
(18) Park, S.-H.; Kleinsorge, M.; Grey, C. P.; Parise, J. B. *J. Solid State Chem.* **2002**, *167*, 310.
(19) Meyer, B.; Leifer, N.; Greenbaum, S.; Grey, C. P. Manuscript in preparation.
(20) Kittel, C. *Introduction to Solid State Physics*, 6th ed.; John Wiley & Sons: New York, 1986.
(21) Carrington, A.; McLachlan, A. D. *Introduction to Magnetic Resonance*; Harper and Row: New York, 1967.
(22) Kohler, F. H. In *Magnetism: Molecules to Materials*; Miller, J. S., Drillon, M., Eds.; Wiley-VCH: New York, 2001.
(23) Albanese, N. F.; Chasteen, N. D. *J. Phys. Chem.* **1978**, *8*, 910.
(24) van Willigen, H. *J. Magn. Reson.* **1980**, *39*, 37.
(25) Atherton, N. M.; Shackleton, J. F. *Mol. Phys.* **1980**, *39*, 1471.
(26) Bertini, I.; Briganti, F.; Luchinat, C.; Xia, Z. *J. Magn. Reson.* **1992**, *99*, 235.
(27) Pan, C. M. A. Thesis, State University of New York at Stony Brook, Stony Brook, NY, 2002.
(28) Marichal, C.; Hirschinger, J.; Granger, P.; Menetrier, M.; Rougier, A.; Delmas, C. *Inorg. Chem.* **1995**, *34*, 1773.
(29) Carlier, D.; Menetrier, M.; Delmas, C. *J. Mater. Chem.* **2001**, *11*, 594.
(30) McConnell, H. M. *J. Chem. Phys.* **1957**, *27*.
(31) McConnell, H. M.; Robertson, R. E. *J. Chem. Phys.* **1958**, *29*, 1361.
(32) Cox, P. A. *Transition Metal Oxides*; Clarendon Press: Oxford, 1995.
(33) Nayeem, A.; Yesinowski, J. P. *J. Chem. Phys.* **1988**, *89*, 4600.
(34) Lee, Y. J.; Grey, C. P. *J. Phys. Chem. B* **2002**, *106*, 3576.
(35) Mehring, M. *Principles of High-Resolution NMR in Solids*; Springer-Verlag: New York, 1983.
(36) Haeberlen, U. *High-Resolution NMR in Solids*; Academic: New York, 1976.
(37) Brough, A. R.; Grey, C. P.; Dobson, C. M. *J. Chem. Soc., Chem. Commun.* **1992**, 742.
(38) Bertini, I.; Luchinat, C.; Parigi, G. *Solution NMR of Paramagnetic Molecules*; Elsevier: Amsterdam, 2001.
(39) Grey, C. P.; Smith, M. E.; Cheetham, A. K.; Dobson, C. M.; Dupree, R. *J. Am. Chem. Soc.* **1990**, *112*, 4670.
(40) Goodenough, J. B. *Magnetism and the Chemical Bond*; Interscience: New York, 1963.
(41) Hatfield, W. E. *Solid State Chemistry Techniques*; Oxford University Press: Oxford, 1987.

(42) Bloembergen, N. *Physica* **1950**, *16*, 95.
(43) Brough, A. R.; Grey, C. P.; Dobson, C. M. *J. Am. Chem. Soc.* **1993**, *115*, 7318.
(44) Lee, Y. J.; Wang, F.; Grey, C. P. *J. Am. Chem. Soc.* **1998**, *120*, 12601.
(45) Lee, Y. J.; Grey, C. P. *Chem. Mater.* **2000**, *12*, 3871.
(46) Lee, Y. J.; Eng, C.; Grey, C. P. *J. Electrochem. Soc.* **2001**, *148*, A249.
(47) Pan, C.; Lee, Y. J.; Ammundsen, B.; Grey, C. P. *Chem. Mater.* **2002**, *14*, 2289.
(48) Gee, B.; Horne, C. R.; Cairns, E. J.; Reimer, J. A. *J. Phys. Chem. B* **1998**, *102*, 10142.
(49) Tucker, M. C.; Reimer, J. A.; Cairns, E. J. *Electrochem. Solid-State Lett.* **2000**, *3*, 463.
(50) Lee, Y. J.; Park, S.-H.; Eng, C.; Parise, J. B.; Toby, B. H.; Grey, C. P. *Chem. Mater.* **2002**, *14*, 194.
(51) Tucker, M. C.; Reimer, J. A.; Cairns, E. J. *J. Electrochem. Soc.* **2001**, *148*, A951.
(52) Carlier, D.; Ménétrier, M.; Grey, C. P.; Delmas, C.; Ceder, G. *Phys. Rev. B* **2003**, *67*, 174103.
(53) Burley, J.; Battle, P. D.; Gallon, D. J.; Sloan, J.; Grey, C. P.; Rosseinsky, M. J. *J. Am. Chem. Soc.* **2002**, *124*, 620.
(54) Greedan, J. E.; Raju, N. P.; Davidson, I. J. *J. Solid State Chem.* **1997**, *128*, 209.
(55) Levasseur, S.; Menetrier, M.; Suard, E.; Delmas, C. *Solid State Ionics* **2000**, *128*, 11.
(56) Lee, Y. J.; Grey, C. P. *J. Electrochem. Soc.* **2002**, *149*, A103.
(57) Verhoeven, V. W. J.; de Schepper, I. M.; Nachtegaal, G.; Kentgens, A. P. M.; Kelder, E. M.; Schoonman, J.; Mulder, F. M. *Phys. Rev. Lett.* **2001**, *86*, 4314.
(58) Morgan, K. R.; Collier, S.; Burns, G.; Ooi, K. *J. Chem. Soc., Chem. Commun.* **1994**, 1719.
(59) Rozier, P.; Savariault, J. M.; Galy, J.; Marichal, C.; Hirschinger, J.; Granger, P. *Eur. J. Solid State Inorg. Chem.* **1996**, *33*, 1.
(60) Stallworth, P. E.; Kostov, S.; denBoer, M. L.; Greenbaum, S. G.; Lampe-Onnerud, C. *J. Appl. Phys.* **1998**, *83*, 1247.
(61) Stallworth, P. E.; Johnson, F. S.; Greenbaum, S. G.; Passerini, S.; Flowers, J.; Smyrl, W.; Fontanella, J. J. *Solid State Ionics* **2002**, *146*, 43.
(62) Gaubicher, J.; Wurm, C.; Goward, G.; Masquelier, C.; Nazar, L. *Chem. Mater.* **2000**, *12*, 3240.
(63) Arrabito, M.; Bodoardo, S.; Penazzi, N.; Panero, S.; Reale, P.; Scrosati, B.; Wang, Y.; Guo, X.; Greenbaum, S. G. *J. Power Sources* **2001**, *97−8*, 478.
(64) Tucker, M. C.; Doeff, M. M.; Richardson, T. J.; Finones, R.; Reimer, J. A.; Cairns, E. J. *Electrochem. Solid State Lett.* **2002**, *5*, A95.
(65) Thackeray, M. M.; David, W. I. F.; Bruce, P. G.; Goodenough, J. B. *Mater. Res. Bull.* **1983**, *18*, 461.
(66) Thackeray, M. M. *Prog. Solid State Chem.* **1997**, *25*, 1.
(67) Gummow, R. J.; de-Kock, A.; Thackeray, M. M. *Solid State Ionics* **1994**, *69*, 59.
(68) Liu, W.; Kowal, K.; Farrington, G. C. *J. Electrochem. Soc.* **1998**, *145*, 459.
(69) Amatucci, G.; Du Pasquier, A.; Blyr, A.; Zheng, T.; Tarascon, J.-M. *Electrochem. Acta* **1999**, *45*, 255.
(70) Cho, J.; Thackeray, M. M. *J. Electrochem. Soc.* **1999**, *146*, 3577.
(71) Shao-Horn, Y.; Hackney, S. A.; Kahaian, A. J.; Kepler, K. D.; Skinner, E.; Vaughey, J. T.; Thackeray, M. M. *J. Power Sources* **1999**, *82*, 496.
(72) Mustarelli, P.; Massarotti, V.; Bini, M.; Capsoni, D. *Phys. Rev. B* **1997**, *55*, 12018.
(73) de-Kock, A.; Rossouw, M. H.; de-Picciotto, L. A.; Thackeray, M. M.; David, W. I. F.; Ibberson, R. M. *Mater. Res. Bull.* **1990**, *25*, 657.
(74) Masquelier, C.; Tabuchi, M.; Ado, K.; Kanno, R.; Kobayashi, Y.; Maki, Y.; Nakamura, O.; Goodenough, J. B. *J. Solid State Chem.* **1996**, *123*, 225.
(75) Xia, Y.; Yoshio, M. *J. Electrochem. Soc.* **1997**, *144*, 4186.
(76) Xia, Y.; Zhou, Y.; Yoshio, M. *J. Electrochem. Soc.* **1997**, *144*, 2593.
(77) Gao, Y.; Dahn, J. R. *J. Electrochem. Soc.* **1996**, *143*, 100.
(78) Paulsen, J. M.; Dahn, J. R. *Chem. Mater.* **1999**, *11*, 3065.
(79) Yamada, A. *J. Solid State Chem.* **1996**, *122*, 160.
(80) Lee, Y.; Wang, F.; Mukerjee, S.; McBreen, J.; Grey, C. *J. Electrochem. Soc.* **2000**, *147*, 803.
(81) Xia, Y.; Yoshio, M. *J. Electrochem. Soc.* **1996**, *143*, 825.
(82) Berg, H.; Kelder, E. M.; Thomas, J. O. *J. Mater. Chem.* **1999**, *9*, 427.
(83) David, W. I. F.; Thackeray, M. M.; de-Picciotto, L. A.; Goodenough, J. B. *J. Solid State Chem.* **1987**, *67*, 316.
(84) Hunter, J. C. *J. Solid State Chem.* **1981**, *39*, 142.
(85) Ooi, K.; Miyai, Y.; Sakakihara, J. *Langmuir* **1991**, *7*, 1167.
(86) Sato, K.; Poojary, D. M.; Clearfield, A.; Kohno, M.; Inoue, Y. *J. Solid State Chem.* **1997**, *131*, 84.
(87) Pickup, D. M.; Simon, D.; Fooken, M.; Krampitz, H.; van Eck, E. R. H.; Kelder, E. M. *J. Mater. Chem.* **2003**, *13*, 963.
(88) Paik, Y.; Osegovic, J. P.; Wang, F.; Bowden, W.; Grey, C. P. *J. Am. Chem. Soc.* **2001**, *123*, 7564.
(89) Paik, Y.; Grey, C. P.; Johnson, C. S.; Kim, J.-S.; Thackeray, M. M. *Chem. Mater.* **2002**, *14*, 5109.
(90) Paik, Y.; Naqvi, N.; Grey, C. P. Unpublished data.
(91) Ronci, L. F.; Stallworth, P. E.; Alamgir, F.; Schiros, T.; van Sluytman, J.; Guo, X.; Reale, P.; Greenbaum, S.; den Boer, M.; Scrosati, B. *J. Power Sources* **2003**, *119*, 631.
(92) Krtil, P.; Dedecek, J.; Kostlanova, T.; Brus, J. *Electrochem. Solid State Lett.* **2004**, *7*, A163.
(93) Ohzuku, T.; Ueda, A.; Yamamoto, N. *J. Electrochem. Soc.* **1995**, *142*, 1431.
(94) Kartha, J. P.; Tunstall, D. P.; Irvine, J. T. S. *J. Solid State Chem.* **2000**, *152*, 397.
(95) Armstrong, A. R.; Bruce, P. G. *Nature* **1996**, *381*, 499.
(96) Capitaine, F.; Gravereau, P.; Delmas, C. *Solid State Ionics* **1996**, *89*, 197.
(97) Bruce, P. G.; Armstrong, A. R.; Gitzendanner, R. L. *J. Mater. Chem.* **1999**, *9*, 193.
(98) Shao-Horn, Y.; Hackney, S. A.; Armstrong, A. R.; Bruce, P. G.; Gitzendanner; Johnson, C. S.; Thackeray, M. M. *J. Electrochem. Soc.* **1999**, *146*, 2404.
(99) Wang, H.; Jang, Y.-I.; Chiang, Y.-M. *Electrochem. Solid State Lett.* **1999**, *2*, 490.
(100) Davidson, I. J.; McMillan, R. S.; Murray, J. J. *J. Power Sources* **1995**, *54*, 205.
(101) Ammundsen, B.; Paulsen, J. M.; Davidson, I. J.; R. S. Liu, R. S.; Shen, C. H.; Chen, J. M.; Jang, Y. J.; Lee, J. *J. Electrochem. Soc.* **2002**, *179*, A431.
(102) Balasubramanian, M.; McBreen, J.; Davidson, I. J.; Whitfield, P. S.; Kargina, I. *J. Electrochem. Soc.* **2002**, *149*, A176.
(103) Gao, Y.; Myrtle, K.; Zhang, M.; Reimers, J. N.; Dahn, J. R. *Phys. Rev. B* **1996**, *54*, 16670−675.
(104) Lu, Z.; Dahn, J. R. *J. Electrochem. Soc* **2002**, *149*, A815.
(105) Lu, Z.; Beaulieu, L. Y.; Donaberger, R. A.; Thomas, C. L.; Dahn, J. R. *J. Electrochem. Soc* **2002**, *149*, A778.
(106) Yoon, W. S.; Paik, P.; Yang, X.-Q.; Balasubramanian, M.; McBreen, J.; Grey, C. P. *Electrochem. Solid State Lett.* **2002**, *5*, A263.
(107) Yoon, W.-S.; Iannopollo, S.; Grey, C. P.; Carlier, D.; Gorman, J.; Reed, J.; Ceder, G. *Electrochem. Solid State Lett.* **2004**, *7*, A167.
(108) Grey, C. P.; Yoon, W. S.; Reed, J.; Ceder, G. *Electrochem. Solid State Lett.* **2004**, *7*, A290.
(109) Menetrier, M.; Saadoune, I.; Levasseur, S.; Delmas, C. *J. Mater. Chem.* **1999**, *9*, 1135.
(110) Siegel, R.; Hirschinger, J.; Carlier, D.; Matar, S.; Menetrier, M.; Delmas, C. *J. Phys. Chem. B* **2001**, *105*, 4166.
(111) Tucker, M. C.; Reimer, J. A.; Cairns, E. J.; Choi, S.; Manthiram, A. *J. Phys. Chem. B* **2002**, *106*, 2842.
(112) Peeters, K. M. P. J.; van Bommel, M. J.; Neilen-ten Wolde, P. M. C.; van Hal, H. A. M.; Keur, W. C.; Kentgens, A. P. M. *Solid State Ionics* **1998**, *112*, 41.
(113) Levasseur, S.; Menetrier, M.; Shao-Horn, Y.; Gautier, L.; Audemer, A.; Demazeau, G.; Largeteaus, A.; Delmas, C. *Chem. Mater.* **2003**, *15*, 348.
(114) Levasseur, S.; Menetrier, M.; Delmas, C. *J. Power Sources* **2002**, *112*, 419.
(115) Alcantara, G. R.; Jaraba, M.; Lavela, P.; Tirado, J. L. *Chem. Mater.* **2003**, 1210.
(116) Carlier, D.; Saadoune, I.; Croguennec, L.; Menetrier, M.; Suard, E.; Delmas, C. *Solid State Ionics* **2001**, *144*, 263.
(117) Gaudin, E.; Taulelle, F.; Stoyanova, R.; Zhecheva, E.; Alcantara, R.; Lavela, P.; Tirado, J. L. *J. Phys. Chem. B* **2001**, *105*, 8081.
(118) Stoyanova, J. R.; Zhecheva, E.; Kuzmanova, E.; Alcantara, R.; Lavela, P.; Tirado, J. L. *Solid State Ionics* **2000**, *128*, 1.
(119) Tucker, M. C.; Doeff, M. M.; Richardson, T. J.; Finones, R.; Reimer, J. A.; Cairns, E. J. *J. Am. Chem. Soc.* **2002**, *124*, 3832.
(120) Padhi, A. K.; Nanjundaswamy, K. S.; Masquelier, C.; Okada, S.; Goodenough, J. B. *J. Electrochem. Soc.* **1997**, *144*, 1609.
(121) Prasad, S. S. In *Handbook of solid-state batteries and capacitors*; Munshi, M. Z. A., Ed.; World Scientific: Singapore, 1995; p 467.
(122) DeSilvestro, J.; Haas, O. *J. Electrochem. Soc.* **1990**, *137*, 5C.
(123) Besenhard, J. O.; Schollhorn, R. *J. Electrochem. Soc.* **1977**, *124*, 968.
(124) Campanella, L.; Pistoia, G. *J. Electrochem. Soc.* **1971**, *128*, 1905.
(125) Dickens, P. G.; Reynolds, G. J. *Solid State Ionics* **1981**, *5*, 331.
(126) Besenhard, J. O.; Heydecke, J.; Fritz, H. P. *Solid State Ionics* **1982**, *6*, 215.
(127) Julien, C.; Khelfa, A.; Guesdon, J. P.; Gorenstein, A. *Appl. Phys.* **1994**, *A59*, 173.
(128) Rehder, D. *Bull. Magn. Reson.* **1982**, *4*, 33.
(129) Mastikhin, V. M.; Lapina, O. B.; Krasilnikov, V. N.; Ivakin, A. A. *React. Kinet. Catal. Lett.* **1984**, *24*, 119.
(130) Zamarev, K. I.; Mastikhin, V. M. *Colloids Surf.* **1984**, *12*, 401.
(131) Fotiev, A.; Slobodin, B. V.; Hodos, M. Y. *Vanadates, their Synthesis, Composition and Properties*; Nauka: Moscow (in Russian), 1988.
(132) Hawthorne, F. G.; Calvo, C. *J. Solid State Chem.* **1977**, *22*, 157.
(133) Fotiev, A. A.; Ivakin, A. A. *Vanadates of Divalent Metals and their Synthesis*; Sverdlovsk (in Russian), 1970.

(134) Muller, D.; Gessner, W.; Grimmer, A. R. *Z. Chem.* **1977**, *B12*, 453.
(135) Klinowski, J. *Prog. NMR Spectrosc.* **1984**, *16*, 237.
(136) Eckert, H.; Wachs, I. E. *J. Phys. Chem.* **1989**, *93*, 6796.
(137) Pletnev, R. N.; Lazukova, N. I.; Gubanov, V. A. *Zh. Fiz. Khim.* **1977**, *51*, 2359.
(138) Gubanov, V. A.; Pletnev, R. N.; Lisson, V. N.; Chirkov, A. K. *Spectrosc. Lett.* **1977**, *10*, 527.
(139) Umeda, J. I.; Kusumoto, H.; Narita, K. *J. Phys. Soc. Jpn.* **1966**, *21*, 619.
(140) Skibsted, J.; Nielsen, N. C.; Bildsoe, H.; Jakobsen, H. *Chem. Phys. Lett.* **1992**, *188*(5−6), 405.
(141) Delmaire, F.; Rigole, M.; Zhilinskaya, E. A.; Aboukais, A.; Hubaut, R.; Mairesse, G. *Phys. Chem. Chem. Phys.* **2000**, *2*, 4477.
(142) Stallworth, P. E.; Johnson, F. S.; Greenbaum, S. G.; Passerini, S.; Flowers, J.; Smyrl, W. *J. Appl. Phys.* **2002**, *92*(7), 3839.
(143) Hirschinger, J.; Mongrelet, T.; Marichal, C.; Granger, P.; Savariault, J.-M.; Déramond, E.; Galy, J. *J. Phys. Chem.* **1993**, *97*, 10301.
(144) Dupré, N.; Gaubicher, J.; Siegel, R.; Brunelli, M.; Hirschinger, J.; Quarton, M. Manuscript in preparation.
(145) Dupré, N.; Gaubicher, J.; Guyomard, D.; Grey, C. P. *Chem. Mater.* **2004**, *16*, 2725.
(146) Murphy, D. W.; Christian, P. A.; DiSalvo, G. J.; Waszczak, J. V. *Inorg. Chem.* **1979**, *18*, 2800.
(147) Whittingham, M. S. *J. Electrochem. Soc.* **1975**, *123*, 315.
(148) Galy, J. *J. Solid State Chem.* **1992**, *100*, 229.
(149) Cocciantelli, J. M.; Doumerc, J. P.; Pouchard, M.; Broussely, M.; Labat, J. *J. Power Sources* **1991**, *34*, 103.
(150) Delmas, C.; Cognac-Auradou, H.; Cocciantelli, J. M.; Menetrier, M.; Doumerc, J. P. *Solid State Ionics* **1994**, *69*, 257.
(151) Bose, M.; Basu, A. *Solid State Ionics* **1986**, *18−19*, 902.
(152) Cocciantelli, J. M.; Suh, K. S.; Senegas, J.; Doumerc, J. P.; Pouchard, M. *J. Phys. Chem. Solids* **1992**, *53*, 57.
(153) Cocciantelli, J. M.; Suh, K. S.; Senegas, J.; Doumerc, J. P.; Soubeyroux, J. L.; Pouchard, M. *J. Phys. Chem. Solids* **1992**, *53*, 51.
(154) Savariault, J. M.; Deramond, E.; Galy, J.; Mongrelet, T.; Hirshinger, J. *Mol. Cryst. Liq. Cryst.* **1994**, *244*, 367.
(155) Galy, J.; Hardy, A. *Bull. Soc. Chim. Fr.* **1964**, *451*, 2808.
(156) Galy, J.; Darriet, J.; Hagenmuller, P. *Rev. Chim. Miner.* **1971**, *8*, 509.
(157) Bonino, F.; Ottaviani, M.; Scrosati B.; Pistoia, G. *J. Electrochem. Soc.* **1988**, *135*, 12.
(158) Pistoia, G.; Pasquali, M.; Tocci, M.; Manev, V. Moshtev, R. V. *J. Power Sources* **1985**, *15*, 13.
(159) de Picciotto, L. A.; Adendorff, K. T.; Liles D. C.; Thackeray, M. M. *Solid State Ionics* **1993**, *62*, 297.
(160) Wadsley, A. D. *Acta Crystallogr.* **1957**, *10*, 261.
(161) Benedek, R.; Thackeray, M. M.; Yang, L. H. *Phys. Rev. B* **1999**, *60−9*, 6335.
(162) Jouanneau, S. These de Doctorat, Universite de Nantes, 2001.
(163) Nanjundaswamy, K. S.; Padhi, A. K.; Goodenough, J. B.; Okada, S.; Ōhtsuka, H.; Arai, H.; Yamaki, J. *Solid State Ionics* **1996**, *92*, 1.
(164) Gaubicher, J.; Le Mercier, T.; Chabre, Y.; Angenault, J.; Quarton, M. *J. Electrochem. Soc.* **1999**, *146*, 4375−4379.
(165) Gaubicher, J.; Chabre, Y.; Angenault, J.; Lautié, A.; Quarton, M. *J. Alloys Compd.* **1997**, *262*, 34.
(166) Dupré, N.; Gaubicher, J.; Le Mercier, T.; Wallez, G.; Quarton, M. *Solid State Ionics* **2001**, *140*, 209.
(167) Dupré, N.; Gaubicher, J.; Angenault, J.; Wallez, G.; Quarton, M. *J. Power Sources* **2001**, *97*, 532.
(168) Jordan, B.; Calvo, C. *Can. J. Chem* **1973**, *51*, 2621.
(169) Gopal, R.; Calvo, C. *J. Solid State Chem.* **1972**, *5*, 432.
(170) Tietze, R. *Aust. J. Chem.* **1981**, *34*, 2035.
(171) Lapina, O. B.; Khabibulin, D. F.; Shubin, A. A.; Bondareva, V. M. *J. Mol. Catal. A* **2000** *162*, 38.
(172) Siegel, R.; Dupré, N.; Quarton, M.; Hirschinger, J. Manuscript in preparation.
(173) Yin, S.-C.; Grondey, H.; Strobel, P.; Huang, H.; Nazar, L. F. *J. Am. Chem. Soc.* **2003**, *125*, 326.